Three dimensional modeling of an solid oxide fuel cell coupling charge transfer phenomena with transport processes and heat generation

Andersson, Martin; Paradis, Hedvig; Yuan, Jinliang; Sundén, Bengt

Published in:
Electrochimica Acta

DOI:
10.1016/j.electacta.2013.08.018

2013

Three Dimensional Modeling of an Solid Oxide Fuel Cell Coupling Charge Transfer Phenomena with Transport Processes and Heat Generation

Martin Andersson*, Hedvig Paradis, Jinliang Yuan, Bengt Sundén

Department of Energy Sciences, Faculty of Engineering,

Lund University, P.O. Box 118, SE- 221 00 Lund, Sweden

* Corresponding author:

martin.andersson@energy.lth.se

Phone: + 46462224908

Fax: +46462224717

Abstract

Fuel cells are promising for future energy systems, because they are energy efficient and able to use renewable fuels. However, there is still a need for improvement and a fully coupled computational fluid dynamics (CFD) approach based on the finite element method, in three-dimensions, is developed to describe an anode-supported planar solid oxide fuel cell (SOFC). Governing equations are solved for electron, ion, heat, gas-phase species and momentum transport, and implemented and coupled to kinetics describing electrochemical reactions.

It is shown that the heat generation due to the electrochemical reactions results in an increased temperature distribution and further current density along the main flow direction. This increase is limited due to the consumption of electrochemical reactants within the cell. For cases with a high current density generation, the resistance to electron transport and the

oxygen gas-phase flow is high for positions (within the cathode) under the interconnect ribs, which gives a high current density gradient in the direction normal to the electrode/electrolyte interface. The increase in the current density is accelerated by an increased temperature along the main flow direction, due to the strong coupling between the local current density and the local temperature. It is shown that an increase of the anode active area-to-volume ratio with a factor of two transfers around 20 mV of (activation) polarization from the anode to the cathode side, for the case investigated in this study.

Keywords: SOFC, FEM, 3D, polarization, electric potential

1 Introduction

It is not an exaggeration to say that almost all problems have multiple scales in nature [1]. The particle size in SOFC functional materials is at the sub-micron scale and the three-phase boundary (TPB) between the solids for the charge transport and the pores for the reactants/products transfer is at the microscale, On the other hand the cell/stack geometries are at the macroscale. The morphology and characteristic properties of these scales are important for the performance of the fuel cell (FC). The sciences at a microscopic scale are critical to the performance at a macroscopic (system) scale. The broad range of the length scales brings about an equally wide range of time scales, with chemical bond vibrations occurring over tens of femtoseconds and, at the other extreme, heating up a stack taking hours. Strong coupling between different transport and reaction phenomena as well as the scales calls for multiphysical computational modeling and simulation of SOFC at multiple scales, which is promising for optimizing the design, as well as to increase the cell/stack performance and the cell lifetime [2].

In situ measurements are often difficult to perform and deliver detailed experimental data, such as local temperature distribution, surface- and gas-phase species distributions or local charge profile. This limitation has resulted in the development of very detailed computational fluid dynamics (CFD)-based models whose ability to predict local and global characteristics for the potential, current density, temperature and concentrations have been demonstrated. The macroscale modeling has gained a lot of success during the last years in understanding complex phenomena occurring during FC operation, and accordingly has enabled improvement of the FC design [2]. It should be noted that CFD models make it possible to reduce the amount of experiments needed for cell development, and only a limited amount of tests is then required to validate the accuracy of the models [3], as revealed in recent reviews on solid oxide fuel cell modeling and development by Grew *et al.* [4] and Andersson *et al.* [5]. One CFD technique is the finite element method (FEM), where the spatial domain is divided into a finite number of volumes or elements. The integral form of the conservation equations is formulated and solved over the prescribed finite volumes. Local conservation of the numerical fluxes is central for FEM. The FEM corresponds to a length scale of 50 μm and bigger as well as a time scale of μs and longer [4]. Various assumptions are often involved in the CFD models, for example, the microstructure of the porous electrodes is not directly included in the model, while the effective parameters, e.g., the porosity, tortuosity factor and the active area-to-volume ratios (AV) for electrochemical reactions, are normally treated as fitting parameters and used in the respective governing equations [6-7].

The Butler-Volmer equations are often used to describe the activation polarization/current density relationship [8]. The exchange current density is frequently used to calculate the activation polarization, which depends on the active catalytic material for the electrochemical reactions. A problem is that the data in literature are not identical or well explained. Further

study of the mechanisms behind the activation polarization is important for the FC development [6,9]. For the anode supported SOFC, the high mechanical strength is maintained for the rest of the anode which is used primarily as the cell support and for internal reforming reactions, when hydrocarbons are supplied as fuels [10-11].

With continuing advances in the development of algorithms and rapid reduction in CPU costs, computational chemistry plays a more and more important role in SOFC electrode design and development. An important new direction for SOFC research is to develop a predictive multiscale (from density functional theory (DFT) to continuum) computational framework, through a rigorous validation at each scale by carefully-designed experiments performed under *in situ* conditions. However, major challenges still remain to bridge the gaps between the models at different scales or between theoretical predictions and experiments [12]. Modeling and simulation across the time and length scales provide unique opportunities to understand properties and phenomena that are inaccessible and difficult to address with experimental effort, or have multifaceted interactions. It is apparent that no single method is suited to studying the full scope of challenges. The scale selected for this study is the cell scale (in 3D), covering one fuel channel as well as one air channel and the corresponding anode, electrolyte, cathode as well as interconnect ribs, i.e., the entire cell length but only 3 % of the cell width (for one cell) is included.

The aim of this paper is to investigate the relationships between the electrochemical active area-to-volume ratios and the current density distribution as well as the couplings between the electrochemical activation energies, the current density distribution and the activation polarizations for an anode-supported planar SOFC. The methodology applied in this study is the FEM. A parameter study is performed varying the cell potential, the anode active area-to-volume-ratio and the electrochemical activation energies, for the objective to identify the

importance of the electrochemical reactions and the effects on the transport phenomena as well as heat generation. Our model makes it possible to identify electron and oxygen ion transport limitations in the direction normal to the cathode/electrolyte interface. Further design optimization is possible based on the local distribution of the different polarizations, ions, electrons as well as gas-phase molecules.

2 Modeling

A three-dimensional (3D) model for an anode-supported planar SOFC is developed and implemented in the commercial software COMSOL Multiphysics (version 4.3.1.161). Equations for ion, electron, momentum, gas-phase species and heat transport are solved simultaneously and coupled to kinetics describing the electrochemical reactions within the electrodes. The geometry and material structure parameters are selected based on a cell developed and tested at the Ningbo Institute of Material Technology and Engineering (NIMTE) in China, as defined in Table 1. The NIMTE cell was further described in [13-14].

Table 1: SOFC cell geometry

Cell Component	Direction	Thickness
Cell length	x	100 mm
Fuel & Air channel height	y	0.5 mm
Fuel & Air channel width	z	2 mm
Channel wall (rib) thickness	z	0.5 + 0.5 mm
Anode support layer thickness	y	400 μm
Anode active layer thickness	y	15 μm
Cathode support layer thickness	y	50 μm
Cathode active layer thickness	y	20 μm
Electrolyte thickness	y	10 μm
Interconnect thickness	y	150 +150 μm

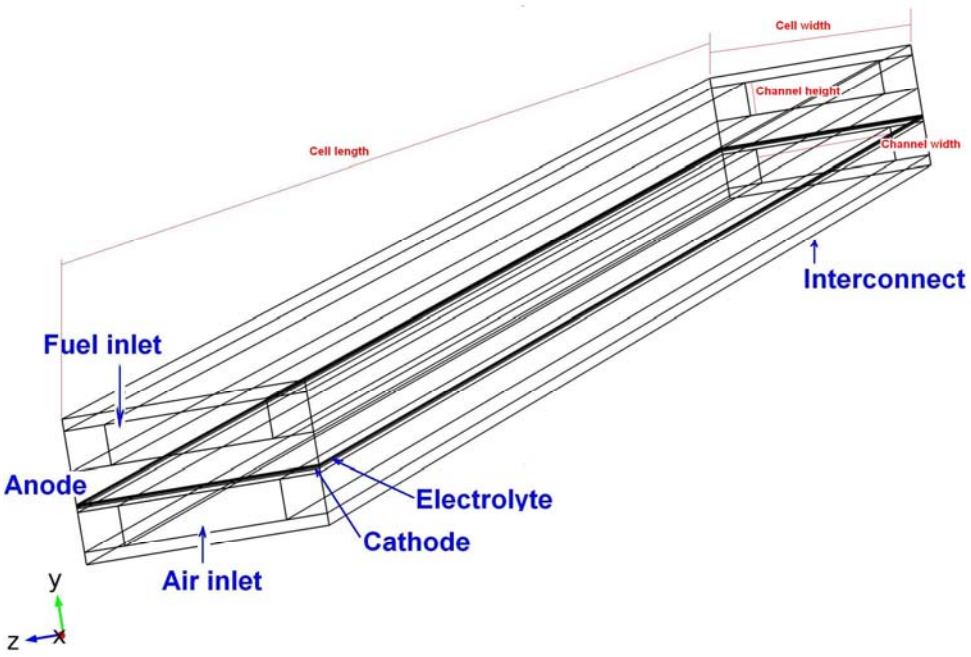

Figure 1. Schematic figure of the anode-supported SOFC model.

If hydrogen is used as a fuel, the active species involved in the electrochemical reactions are hydrogen and oxygen, as shown in eqns (1)-(2). H_2 forms a molecule of H_2O during this oxidation reaction and releases a pair of electrons [15-16]. The electrochemical reactions occur at the three-phase boundaries (TPBs), i.e., the region where the ionic (YSZ), electronic (Ni or LSM) conducting materials and gas-phase meet each other. Oxygen ions migrate in the YSZ material (from the cathodic side to the anodic side through the electrolyte layer), conduction of electrons occurs in the electronic-phase (Ni in the anode or LSM in the cathode) and transport of gas molecules takes place in the open voids within the electrodes. Note that the TPB needs to be connected to the rest of the porous domains, i.e., the pores need to be connected through the surrounding pore network to the fuel/air stream, the Ni- or LSM-phase must be connected to the respective current collector and the YSZ-phase in the electrodes to the YSZ electrolyte for the electrochemical reactions to proceed [17].

$$\frac{1}{2}O_2 + 2e^- \Leftrightarrow O^{2-} \quad (1)$$

$$H_2 + O^{2-} \Leftrightarrow H_2O + 2e^- \quad (2)$$

2.1 Governing equations

2.1.1 Ion and electron transport as well as electrochemical reactions

The rate at which the current within the electrodes can transfer between ionic and electronic phases is dependent on several factors, such as the catalytic activity of the materials, the extension of the reaction region as well as the relative facility at which charges and chemical species are transported to and from the reaction sites. Further, these depend on the microstructural characteristics of the electrodes, such as porosity, particle size and material composition. The interactions between materials, catalytic activity, microstructure characteristics and geometrical structure play a significant role for the efficiency of the electrode [18]. It was concluded, by Bertei *et al.* [18], that the cathode become less conductive and offers a smaller density of reacting sites as the thickness increases when a linearly distributed (graded) porosity was implemented. Thin electrodes only have a limited amount of TPB length available. This limits an effective conversion of the electrochemical reactants due to the lack of reaction sites and leads to a high activation polarization. Thick electrodes are less conductive even if they offer a larger TPB length, because the performance is often limited by the charge transport. Bertei *et al.* showed that distributed porosity and thickness mainly led to a decrease of the effective properties of the conducting phases (such as density of reaction sites, TPB length, effective electronic and ionic conductivities) as the thickness of the cathode was increased.

In general, the intrinsic material conductivities can be obtained by using direct experimental measurements. But, quantification of the porous microstructures and the effects on the properties of the porous electrodes are difficult, especially when the material features of the porous electrode are not known before hand. Shi and Xue [19] developed an inverse approach to determine the extra parameters needed using experimental measurements of cell polarization performance in an optimization procedure, and concluded that the cell performance is very sensitive to reference exchange current densities, which are related to catalytic property of the electrode. The cell performance was moderately sensitive to porous microstructure parameters and not sensitive to the permeability of the electrodes.

Due to internal resistance and polarizations (overpotential losses) the actual potential (E) becomes less than the equivalent equilibrium potential under working conditions (or ideal condition potential, E^{ICV}). The actual potential can be expressed as [20]:

$$E = E^{ICV} - |\eta_{act}| - \eta_{ohm} - \eta_{conc} \tag{3}$$

Here, η are the respective polarizations. The activation polarizations in the electrodes are defined as:

$$\eta_{act,a} = \phi_s - \phi_l \tag{4}$$

$$\eta_{act,c} = \phi_s - \phi_l - E^{ICV}_{H_2/O_2} \tag{5}$$

where ϕ is the local potential. The index a stands for the anode, c for the cathode, s for the electron transfer material and l for the ion transfer material. It should be mentioned that ϕ_l is positive within both the anode and cathode, while ϕ_s is positive in the cathode and negative in the anode.

The influence of different potentials/polarizations varies depending on cell operating conditions and design/structure. The local potentials vary between different positions (in 3D) within the cell and they are affected by, for example, the local hydrogen and oxygen concentrations, the local temperature as well as the ion and electron transport path. It is found in Sohn *et al.* [21] that for a co-flow anode-supported planar SOFC, the activation polarization is dominant in the cathode near the fuel and air inlets, and in the anode near the outlets. Also the counter-flow configuration was investigated and the variation in the cathodic activation overpotential is smaller. For both the co- and the counter-flow configurations the activation polarization in the cathode is dominating at lower current densities and the activation polarization in the anode at higher ones. The dominance of the anode activation at high current densities is explained by the depletion of hydrogen due to the fuel utilization [21]. The influence on the charge transfer losses, η_{ohm}, depends mostly on the ion conductivity within the electrolyte materials in the electrodes and the electrolyte thickness, where a decreased thickness result in a decreased ohmic polarization. When the concentration of oxygen or hydrogen reaches zero at the TPB (for example for positions under the interconnect ribs), the concentration polarization increases and the ICV decreases, i.e., the current reaches zero [22]. Bessler *et al.* [23] studied an electrode-supported SOFC and concluded that the polarizations within the cathode are small compared to the one within the anode or electrolyte. Xiao *et al.* [24] investigated an anode-supported SOFC with a Ni/YSZ anode and an LSM cathode and found that the cathodic polarization decreased off increasing temperature, but the anodic polarization increased off increasing temperature, partly due to an increase in the resistivity of the Ni/YSZ cermet connected to the drop in metallic conductivity as the temperature increases.

The concentration polarizations are specified as [25]:

$$\eta_{conc,a} = \frac{\mathrm{R} \cdot T}{n_{e,a} \cdot \mathrm{F}} \ln\left(\frac{p_{H_2O,TPB} \cdot p_{H_2,b}}{p_{H_2,TPB} \cdot p_{H_2O,b}} \right) \tag{6}$$

$$\eta_{conc,c} = \frac{\mathrm{R} \cdot T}{n_{e,c} \cdot \mathrm{F}} \ln\left(\frac{p_{O_2,b}}{p_{O_2,TPB}} \right) \tag{7}$$

Here, p is the partial pressure at the *TPB* or *b* (bulk fluid within the gas channels). It should be mentioned that eqns (6)-(7) are developed for equilibrium conditions and the development and implementation of more accurate expression is interesting for future work. The relative importance for the different polarizations is discussed in section 3 and 4.

The electromotive force (equivalent equilibrium potential under working conditions (E^{ICV})) is determined by the difference in the thermodynamic potentials of the electrode reactions. When a hydrogen-steam mixture is used as fuel, it can be calculated by the Nernst equation (eqn (8)) [26-27].

$$E^{ICV}_{H_2/O_2} = E^0_{H_2/O_2} - \frac{\mathrm{R} \cdot T}{2 \cdot \mathrm{F}} \cdot \ln\left(\frac{p_{H_2O,TPB}}{p_{H_2,TPB} \sqrt{p_{O_2,TPB}}} \right) \tag{8}$$

$$E^0_{H_2/O_2} = 1.253 - 2.4516 \cdot 10^{-4} \cdot T \tag{9}$$

where E^0 is the temperature dependent open-circuit potential at standard pressure and p_i the partial pressure, at the TPB, in atm.

The current density can be obtained through the Butler-Volmer equation [28-29]. It is common to assume symmetric electron transfer in the Butler-Volmer equation (i.e., the transfer coefficient is assumed to be 0.5 [30]), and this often agrees well with experimental Tafel plots. The Butler-Volmer equation is then reduced to eqn (10). Assuming singe-step rate limiting reaction for two electrodes, that the sum of the potential must equal the Nernst

potential and that the transfer coefficient is 0.5, the following relationships apply: $i_0 \propto p_{O_2}^{0.25}$ at the cathode and $i_0 \propto p_{H2_2}^{0.5} p_{H_2O}^{0.5}$ at the anode [30]. The activation overpotential is mainly important at small currents and has roughly the magnitude of the thermal voltage (kT/e). At larger currents, the activation overpotential grows much more slowly, as a logarithm of the applied current (relative to the exchange current) [31].

$$i = 2 \cdot AV \cdot i_0 \cdot \sinh\left(\frac{n_e \cdot \mathrm{F} \cdot \eta_{act,e}}{2 \cdot \mathrm{R} \cdot T}\right) \tag{10}$$

$$i_0 = \frac{\mathrm{R} \cdot T}{n_e \cdot \mathrm{F}} \cdot k_e'' \cdot \exp\left(\frac{-E}{\mathrm{R} \cdot T}\right) \tag{11}$$

where i is the current density, F Faraday's constant, k_e'' the pre-exponential factor (which is $6.54 \cdot 10^{11}$ $\Omega^{-1}m^{-2}$ for the anode and $2.35 \cdot 10^{11}$ $\Omega^{-1}m^{-2}$ for the cathode [7]), i_0 the exchange current density, n_e the number of electrons transferred per reaction (=4 in the cathode and 2 in the anode), R the ideal gas constant and AV the electrochemical active area to volume ratio [7]. An activation energy ($E_{a,e}$) of 137 kJ/mol for the cathode and 140 kJ/mol for the anode are used by Patcharavorachot *et al.* [20] and Aguiar *et al.* [22] as well as in this work, while the values between 130 and 190 kJ/mol for the cathode and 110 and 140 kJ/mol for the anode appeared in various work available in the open literature [32-36]. The large activation energies discrepancies in the open literature are the reason conducting the parameter study.

The heat generation by the electrochemical reactions and due to the losses through the activation, the ohmic and the concentration polarizations is given by [25]:

$$Q_h = |i| \cdot \left(\frac{T \cdot |\Delta S_r|}{n_e \cdot \mathrm{F}} + |\eta_{act}| + \eta_{conc} \right) + \sum \frac{i^2}{\sigma} \tag{12}$$

Here, i is the current density, σ is the ion/electron conductivity, Q_h is the heat generation/consumption and ΔS_r is the entropy change of the electrochemical reactions, calculated from the data in [37] for the anode and the cathode TPBs, respectively.

The potential difference between the anode and the cathode current collectors corresponds to the total cell operating potential. The governing equations for the ion and electron transport are implemented according to eqns (13)-(14).

$$i_l = \nabla \bullet \left(-\sigma_l \nabla \phi_l \right) \tag{13}$$

$$i_s = \nabla \bullet \left(-\sigma_s \nabla \phi_s \right) \tag{14}$$

where ϕ is the potential. The electronic conductivities in the anode ($\sigma_{s,a}$) and the cathode ($\sigma_{s,c}$), and ionic conductivity in the YSZ ($\sigma_{l,el}$) can be calculated as [38,39]:

$$\sigma_{s,a} = \frac{9.5 \cdot 10^7}{T} \cdot \exp\left(\frac{-1150}{T} \right) \tag{15}$$

$$\sigma_{s,c} = \frac{4.2 \cdot 10^7}{T} \cdot \exp\left(\frac{-1200}{T} \right) \tag{16}$$

$$\sigma_{l,el} = 3.34 \cdot 10^4 \cdot \exp\left(\frac{-10300}{T} \right) \tag{17}$$

The actual length that ions and electrons are transported in the electrodes increases because of the real material compositions and their micro porous structures. This is accounted for by using the structure-dependent tortuosity factors (τ = square of tortuosity) and volume

fractions (eqns (18)-(20)). The effective ionic- and electronic conductivities in the electrodes are defined as [40]:

$$\sigma_{l,e,YSZ} = \sigma_{l,e} \cdot \frac{V_{YSZ,e}}{\tau_{YSZ,e}} \tag{18}$$

$$\sigma_{s,a,Ni} = \sigma_{s,a} \cdot \frac{V_{Ni,a}}{\tau_{Ni,a}} \tag{19}$$

$$\sigma_{s,c,LSM} = \sigma_{s,c} \cdot \frac{V_{LSM,c}}{\tau_{LSM,c}} \tag{20}$$

where V is the volume fraction for the specific materials in the electrodes.

2.1.2 Momentum transport

The governing equations for momentum transport are normally the Navier-Stokes equations in the fuel channels and the Darcy equation for the porous electrodes [41-42]. The physics of laminar and turbulent incompressible flow are well described by the Navier-Stokes equation, and it is common practice to assume laminar flow for fuel cell gas channels due to the low velocities, which decreases the computational cost significantly [43]. The Darcy equation describes the balance between the force from the pressure gradient and the frictional resistance from the (porous) solid material. It should be noted that the Darcy equation expresses the flow in the porous structure well away from the walls. It is found that the conditions at the fuel and air channel-electrode interfaces are not well described by either the Darcy or the Navier-Stokes equations. Equation (21) is developed and implemented by COMSOL Multiphysics to enable continuous velocity and pressure fields, i.e., the channel and the porous region is treated as a single domain [44-45].

$$\left(\frac{\mu}{\kappa}+\rho\cdot\nabla\bullet\vec{\mathrm{u}}\right)\cdot\vec{\mathrm{u}}-\nabla\left[-p+\frac{1}{\varepsilon}\left\{\Psi-\left(\frac{-2}{3}\cdot\mu\right)(\nabla\bullet\vec{\mathrm{u}})\right\}\right]=\mathbf{F} \tag{21}$$

where $\mathbf{F}$ is the volume force vector, p the pressure, κ the permeability of the porous medium ($1.76\cdot10^{-11}$ m^2 [15]), $\vec{\mathrm{u}}$ the velocity vector, Ψ the viscous stress tensor. The momentum equation in the air and fuel channels reduces to eqn (22).

$$\rho\cdot(\nabla\bullet\vec{\mathrm{u}})\cdot\vec{\mathrm{u}}-\nabla\left[-p+\mu\cdot\left\{\Psi-\frac{2}{3}\cdot(\nabla\bullet\vec{\mathrm{u}})\right\}\right]=\mathbf{F} \tag{22}$$

The viscosity (μ) and density (ρ) for the participating gas mixtures are dependent on local temperature and mole fractions [7]:

$$\rho_g=\frac{p\cdot\sum x_j\cdot M_j}{\mathrm{R}\cdot T} \tag{23}$$

$$\mu_j=\sum_{k=1}^{7}\mathrm{b_k}\cdot\left(\frac{T}{1000}\right)^k \tag{24}$$

$$\mu_g=\sum_i x_j\cdot\mu_j \tag{25}$$

where x_j is the mole fraction of gas-phase species j, $\mathrm{b_k}$ the species dependent parameter and "k" stands for the number of species dependent parameters in the equation and index g is the gas-phase.

2.1.3 Mass transport

In the porous electrodes, there are two kinds of gas-phase species diffusion mechanisms; Knudsen (collisions between the gas molecules and the pore walls) and molecular (collisions between two different gas molecules) diffusions. The Knudsen diffusion coefficient of the component *i* with the component *j* in a gas mixture, $D_{k,ij}$, is calculated based on the free molecule flow theory, as described in [7]. For a multi-component gas mixture system, the temperature dependent binary diffusion coefficients (D_{ij}) are calculated by the expressions in [46], based on bi-component coefficients of the gases. In the porous media, there is an increased diffusion length due to the tortuous paths of connected real pores and the coefficients are usually corrected by tortuosity factor and porosity [47]. LBM was used by Kanno *et al*. [48] to calculate the tortuosity factors and values between 6 and 14 are found for YSZ, between 7 and 17 for Ni as well as between 2 and 2.4 for gas-phase pore transport, respectively. The random walk process of nonsorbing particles as well as the LBM method was used by Iwai *et al*. to evaluate the tortuosity factors and values between 6.91 and 29.46 were found for Ni, between 9.84 and 27.89 for YSZ as well as between 1.78 and 2.06 for gas-phase pore transport, respectively. The variations are explained by different evaluation methods and by the direction (x, y and z) [49]. Vivet *et al.* [50] calculated the tortuosity in the range of 3.04 and 6.24 for Ni, and between 1.79 and 2.10 for YSZ, respectively. Aguiar *et al.* [22] uses a gas-phase pore tortuosity factor of 6 and Bessler *et al.* [23] uses a gas-phase pore tortuosity factor of 3.5., in their respectively models. For this work the dimensionless parameters for the electrode structure stated in Table 2 are employed. Equation (26) is used to describe the gas-phase species transport phenomena for each component inside the cell [45] and solved for the air- and fuel channels and the electrodes.

$$\nabla\left(-\rho\cdot w_i\sum^{n}D_{eff,ij}\cdot\nabla x_j+\left(x_j-w_j\right)\frac{\nabla p}{p}\bullet\vec{\mathrm{u}}-D_i^T\cdot\frac{\nabla T}{T}\right)+\rho\cdot\vec{\mathrm{u}}\cdot\nabla w_j=S_i \qquad (26)$$

where T is the temperature, w the mass fraction, D_i^T the thermal diffusion coefficient (assumed to be zero in this work) and S_i the source term due to electrochemical reactions. The mass transport consists of several parts, i.e., convective, diffusive and thermal. The convective mass transport occurs due to the movement of the bulk fluid, i.e., the pressure differences from the inlet to the outlet. Diffusive mass transport makes molecules move from higher to lower concentrations, i.e., to and from the TBP layers. Thermal diffusion moves molecules, due to temperature gradients. The relative magnitude of the diffusive and convective mass transport depends on the direction (main flow direction, direction through the electrode/electrolyte interface and the direction normal to the electrode/electrolyte interface). The gas flow in the main flow direction is driven by the convective flow from the inlet to the outlet. On the air side diffusive transport takes place, due to the concentration gradients but also a small pressure gradient occur in the directions through the electrode/electrolyte interface as well as normal to the electrode/electrolyte interface, due to the consumption of oxygen molecules, which enables convective mass transport in these directions. On the fuel side, one mole of hydrogen produce one mole of water in the electrochemical reactions, i.e., the mass transport in the direction through the electrode/electrolyte interface as well as normal to the electrode/electrolyte interface is dominated by diffusion.

2.1.4 Heat transport

A local temperature equilibrium (LTE) approach is applied, i.e., the temperature is assumed to be locally the same for the solid- and gas-phases (within the electrodes). The equation 27 is formulated generally and implemented for the complete domain. It reduces to pure heat conduction in the electrolyte layer and in the interconnector, where the gas velocity is zero, i.e., the convective term in the equation does not contribute to the heat transfer. On the other

hand, the velocity in the channels and electrodes is not zero, and contributes to the convective heat transfer.

$$\rho_g \cdot c_{p,g} \cdot \vec{u} \cdot \nabla T = \nabla \bullet \left(k_{eff} \nabla T\right) + Q_h \tag{27}$$

Here k_{eff} is the effective thermal conductivity (defined in eqn (28) [10]) and c_p the gas-phase specific heat.

$$k_{eff} = \varepsilon_p \cdot k_g + (1-\varepsilon) \cdot k_s \tag{28}$$

The specific heat for each gas species *i* and the gas mixture is calculated as [51]:

$$c_{p,i} = \sum_{k=1}^{7} a_k \cdot \left(\frac{T}{1000}\right)^k \tag{29}$$

$$c_{p,g} = \sum_i x_i \cdot c_{p,i} \tag{30}$$

where a_k is the species dependent parameter (extracted from [51]) and "k" stands for the number of parameters involved in the specific heat calculation. The thermal conductivity for each species of the gas-phase *i*, as well as for the gas mixture, is defined as [51]:

$$k_i = 0.01 \cdot \sum_{k=1}^{7} c_k \cdot \left(\frac{T}{1000}\right)^k \tag{31}$$

$$k_g = \sum_i x_i \cdot k_i \tag{32}$$

where c_k is the species dependent parameter (extracted from [51]) and "k" stands for the number of parameters in the thermal conductivity evaluation.

Some of the cell parameters used are given in Table 2 and the solid material parameters in Table 3.

Table 2: SOFC modeling parameters

Inlet temperature	1000 K
Flow arrangement	co-flow
Ion conducting volume fraction	0.42
Electron conducting volume fraction	0.28
Porosity	0.30
Ion conducting tortuosity	10
Electron conducting tortuosity	10
Gas-phase tortuosity	3
Cell voltage	0.7 V
Average pore radius	0.34 μm

Table 3: Solid Material Parameters

	Thermal conductivity [S. Kakaç, A. Pramuanjaroenkij, X.Y. Zhou., A Review of Numerical Modeling of Solid Oxide Fuel Cells, J. Hydrogen Energy 32 (2007) 761-786.] **(W/m/K)**	**Specific heat** [V. Janardhanan, O. Deutschmann, CFD Analysis of a Solid Oxide Fuel Cell with Internal Reforming: Coupled Interactions of Transport, Heterogeneous Catalysis and Electrochemical Processes, J. Power Sources 162 (2006) 1192-1202.] **(J/kg/K)**
Anode (Ni/YSZ)	11	450
Cathode (LSM/YSZ)	6	430
Electrolyte (YSZ)	2.7	470
Interconnect (stainless steel)	20	550

2.2 Boundary conditions

The gas inlet velocities are defined as a laminar flow profile, and the average values are based on the hydrogen- and oxygen utilization, i.e., 76 % and 12 %, respectively, for the standard case in this study. At the outlets the pressure (1 atm) is fixed. The fuel inlet fractions are defined as 90 % (mole) hydrogen and 10 % (mole) water. The air (inlet) includes oxygen and nitrogen. The boundary conditions for the channel outlets are defined as convective flux. The inlet gas temperature is defined by the operating temperature (1000 K) and the outlet is defined as a convective flux. The boundaries at the top and the bottom of the cell are defined as symmetry conditions, because it is assumed that the cell is surrounded by other ones with identical temperature distribution. The potential at the anode current collector is set to zero and the potential at the cathode current collector is set as the cell operating potential (0.7 V for the standard case in this study). All other boundaries and interfaces are electrically insulated.

2.3 Definition of parameter study

The simulation is conducted for five cases:

- Standard case with specified fuel and oxygen utilizations (see section 2.2).
- The cell potential is decreased from 0.7 to 0.675 V, compared to the standard case.
- The active area-to-volume ratio available for the anodic electrochemical reaction is increased by a factor of two, compared to the standard case.
- The anode activation energy for the electrochemical reaction is decreased from 140 kJ/mol to 133 kJ/mol, compared to the standard case.
- The cathode activation energy for the electrochemical reaction is decreased from 137 kJ/mol to 130 kJ/mol, compared to the standard case.

It should be noted that only one parameter is varied (compared to the standard case) in each step within the parameter study.

2.4 Grid independence test

The governing equations are segregated in 5 different groups: 1. velocity field, pressure distribution and pressure corrections, 2. temperature distribution, 3. ion and electron distribution, 4. mass fraction distribution on the air side (O_2/N_2) and 5. mass fraction distribution on the fuel side (H_2/H_2O). The segregated solver solves for 9 279 000 degrees of freedom and the tolerance is defined to 0.0005 for each segregated group. Grid independence was achieved at 1 399 000 elements, after which the change (for the standard case) in the maximum temperature is less than 0.05 %, in the maximum air velocity less than 0.01 %, in the oxygen consumption less than 0.17 % and in the maximum current density less than 0.02 % (compared with the predictions by 2 083 000 elements). It should be noted that the mesh is finest close to the electrode/electrolyte interface and coarsest for the air- and fuel channels and for interconnects. The reason for such a mesh arrangement is mainly due to the fact that the charge transport and the electrochemical reactions (affecting the governing transport equations for ion, electron, mass, heat and momentum) appear only in the regions close to the electrode/electrolyte interface. The calculation time is in the order of some days on a single computer with 16 GB RAM and a CPU with 3.40 GHz.

3 Results and discussion

3.1 Standard case

The temperature profile is shown in Fig. 2. The temperature increases along the main flow direction because the electrochemical reactions as well as the activation, ohmic and concentration polarizations generate a significant amount of heat. The degree of temperature increase is managed with the oxygen utilization, i.e., the inlet (average) air velocity. The change in entropy to electrochemical corresponds to 45 % of the total heat generation,

compared to 29 % from the activation polarization, 20 % from the ohmic polarization due to ion transport, 3.5 % from concentration polarization and 2.8 % from ohmic polarization due to electron transport. Note that the local fractions of the different sources of heat generation differs significantly from the just mentioned average values. It should be mentioned that an LTE approach is applied in the current study and the temperature is assumed to be the same in the gas- and solid phase at each specific position.

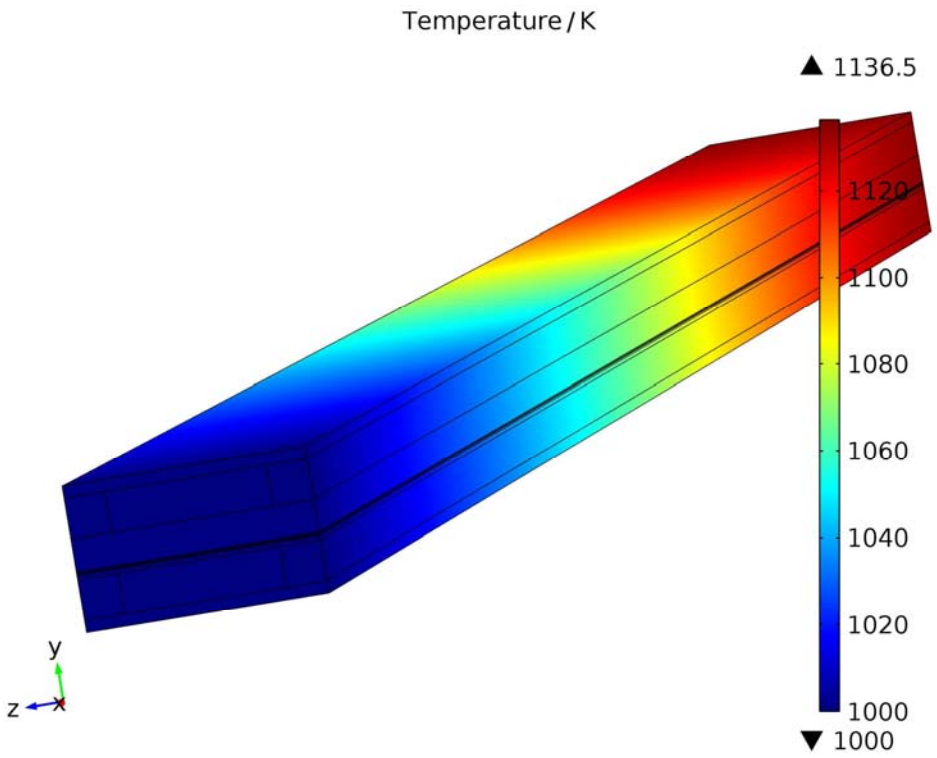

Figure 2. Temperature distribution for the standard case.

The mole fraction of oxygen is presented in 3D in Fig 3. Oxygen is the reactant in the electrochemical reactions at the cathodic TPB. The oxygen mole fraction gradient in the direction normal to the main flow direction (z-direction) is significant, due to the effects of the ribs (interconnect between the channels) on the mass flow resistance. Note, that this effect was not possible to identify in our previous 2D models [2,7,10,25], as this direction was neglected. To decrease this remarkable mole fraction gradient, the cathode support layer can

be manufactured with bigger pore radii compared to the ones for the cathode active layer, or the interconnect thickness between two air channels can be made thinner. However, such investigations are outside the scope of this paper. Our findings in the current work can be compared to similar ones revealed in an earlier work by Kenny and Karan [52], where their predictions showed that the cathode performance can be enhanced upon addition of a current collector layer, due to better oxygen distribution underneath the interconnect, i.e., in the direction normal to the electrode/electrolyte interface. Kenny and Karan concluded that changing one of the microstructural or geometric parameters affect the transport of ions, electrons as well as gas-phase oxygen molecules, i.e., it is critical to consider all aspects of the coupled reaction-transport processes in optimizing the electrodes for improved structures. However, their model was developed in 2D only considering the cathode, compared to 3D and a complete structure of the cell in this work.

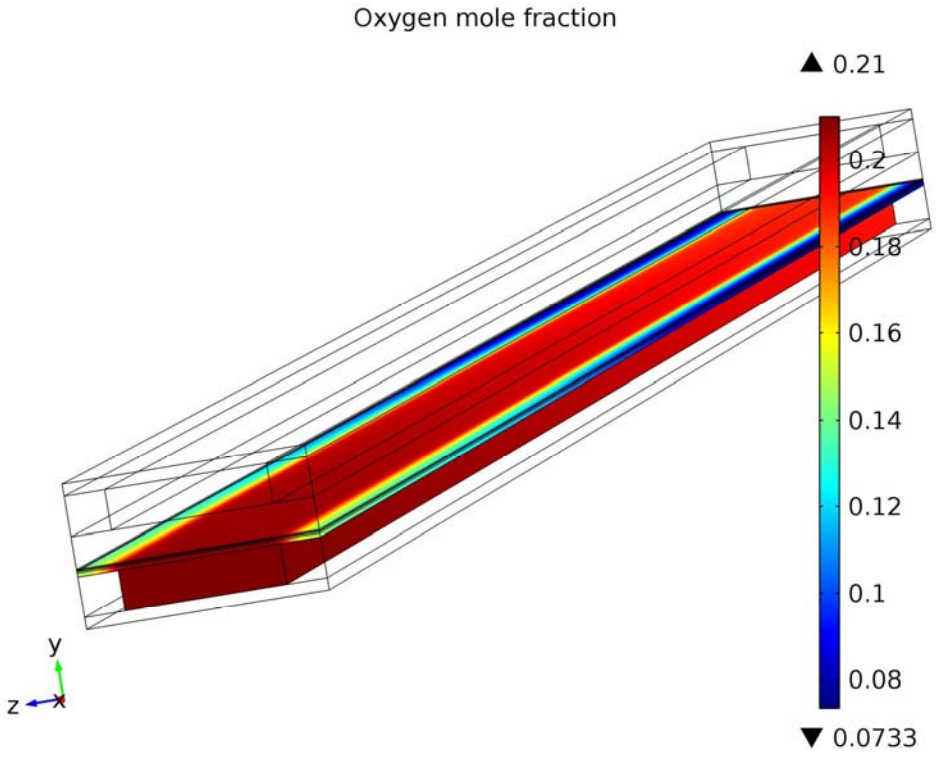

Figure 3. Oxygen mole fraction distribution for the standard case.

The mole fraction of hydrogen (Fig. 4) decreases along the main flow direction, due to the electrochemical reactions at the anode TPB. The relatively thick anode (415 μm) enables easy transport of hydrogen to the TPB (and water from the TPB), also at positions under the interconnect ribs, i.e., the mole fraction gradient in the direction normal to the electrode/electrolyte interface (z-direction) is relatively small (compared to the situation with oxygen distribution in Fig. 3). Besides hydrogen only water is included in the anodic mass transport equation.

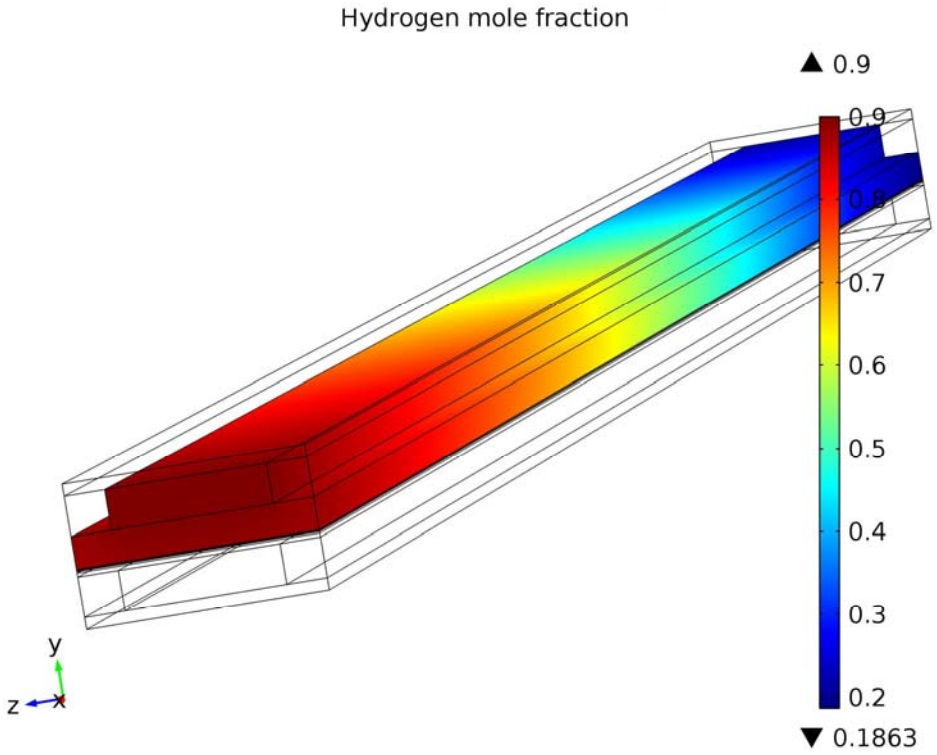

Figure 4. Hydrogen mole fraction distribution for the standard case.

The current density distribution at the cathode/electrolyte interface is presented in Fig. 5. Note that the scales on the axes are made dimensionless according to eqns. (33)-(34). It should be noted that the color scale is identical for all figures presenting the current density (in the z-x-plane), i.e., only approximately three-fourth of the color scale is used for Fig. 5. The average current density for the standard case reaches 2170 A/m^2 (which corresponds to a power density of 1520 W/m^2). The current density increases along the main flow direction (x*-direction in Fig. 5) as the temperature rises. This increase is limited due to the

consumption of oxygen and hydrogen by the electrochemical reactions as well as the production of water. In the direction normal to the main flow direction (z*-direction in Fig. 5) the current density is highest close to the channel/interconnect interfaces where the electron transport distance is short and the concentration of oxygen is high. Note that this was not possible to demonstrate in our previous 2D models. Notice that our average current densities (or power densities) are slightly lower compared to the (published) experimental data. The reason is that the area-to-volume ratios origin from the development of our previous 2D models [7,10] (validated by the experimental data from NIMTE). The current density is decreased (compared to the 2D model) because mass and electron transport limitations occur in the direction normal to the electrode/electrolyte interface (this direction was not captured in the 2D models) as well as 3D effects of the fluid flow, which decreases the flow rate to the positions close to the walls in the direction normal to the electrolyte/electrode interface. However, it is relatively easy to increase the current generation in the model by increasing the electrochemical active area-to-volume ratios (performed in the parameter study) and/or decreasing the electrochemical activation energy (performed in the parameter study). Notice, that the range of published electrochemical activation energy data is several times bigger than what is investigated in our parameter study.

$$x^* = x / L \tag{33}$$

$$z^* = z / W \tag{34}$$

Here, W is the width of one fuel/air channel and the corresponding ribs (=3 mm) as well as L is the cell length along the main flow direction (=100 mm).

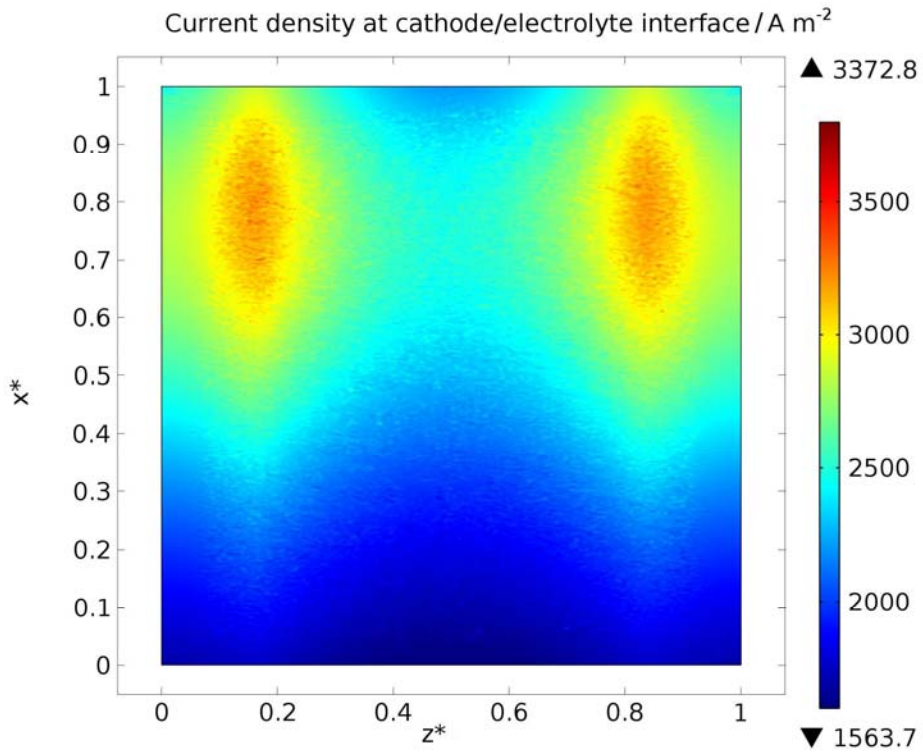

Figure 5. Ion current density for the standard case. (0) at the x*-axis corresponds to the inlet and (1) to the outlet. (0.167) and (0.833) at the z*-axis corresponds to the electrode/channel interfaces.

The ICV at the cathode/electrolyte interface (Fig. 6) is highest close to the inlet, where the temperature and the concentration of water are the lowest as well as the concentration of hydrogen and oxygen are the highest. The ICV decreases along the main flow direction (x*-direction in Fig. 6) due to the ongoing electrochemical reactions and the increased temperature. The ICV gradient in the direction normal to the main flow direction (z*-direction in Fig. 6) occurs due to the oxygen mole fraction gradients within the cathode in this direction, as discussed earlier. It should be mentioned that the color scale is identical for all figures presenting the ICV in the z-x-plane, i.e., only around three-fourth of the color scale is used for Fig. 6.

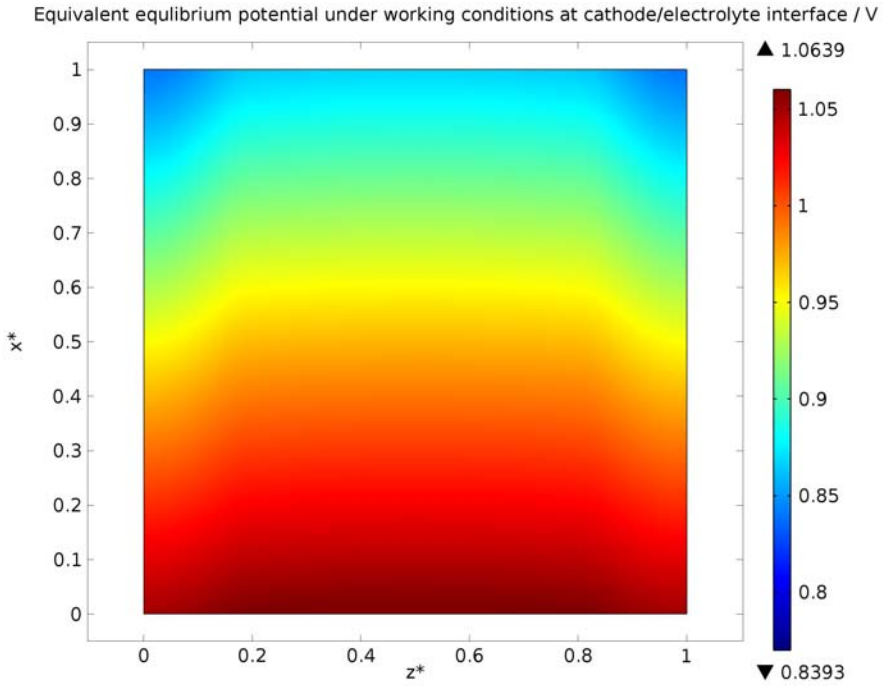

Figure 6. ICV for the standard case. (0) at the x*-axis corresponds to the inlet and (1) to the outlet. (0.167) and (0.833) at the z*-axis corresponds to the electrode/channel interfaces.

The anode activation polarization at the anode/electrolyte interface is presented in Fig. 7 and the cathode one at the cathode/electrolyte interface is presented in Fig. 8. Note that the color scale is identical for all figures presenting the anode as well as cathode activation polarization (in the z-x-plane). It is clear that the activation polarizations are highest at the inlet, corresponding to a high ICV according to eqns (4)-(5) and (8)-(9). The activation polarization gradient in the direction normal to the main flow direction (z*-direction) is coupled to the ICV gradient in the same direction, but depends also on the concentration and ohmic polarizations. The model presented in this paper predicts a slightly higher activation polarization within the anode, compared to the one in the cathode. The difference between activation polarizations in the anode and cathode sides decreases along the main flow direction. Note that the current density and the activation polarizations are highest at the electrode/electrolyte interface and decreases rapidly within the electrodes as the distance to the interface increases (note that this direction is not shown in Figs 7-8). On the other hand, the ohmic polarization increases at positions far from the interface.

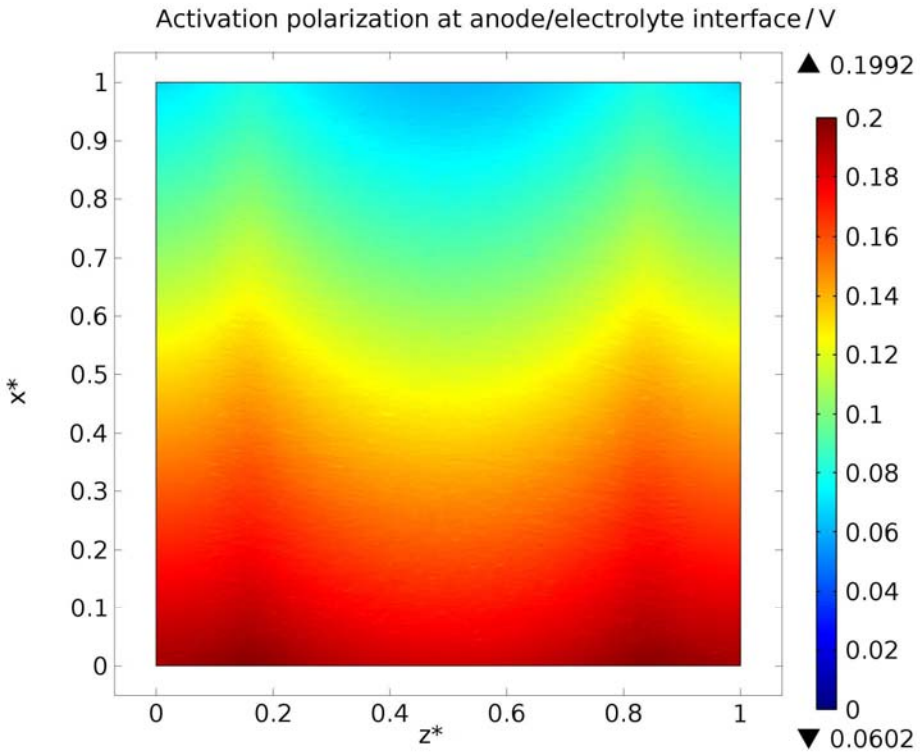

Figure 7. Activation polarization at the anode/electrolyte interface for the standard case. (0) at the x*-axis corresponds to the inlet and (1) to the outlet. (0.167) and (0.833) at the z*-axis corresponds to the electrode/channel interfaces.

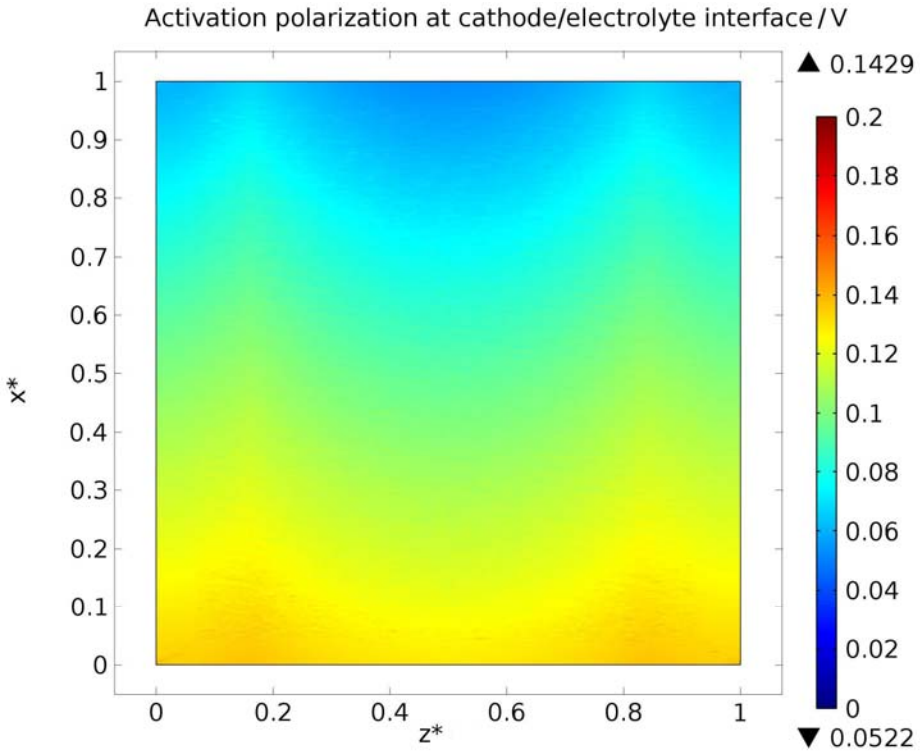

Figure 8. Activation polarization at the cathode/electrolyte interface for the standard case. (0) at the x*-axis corresponds to the inlet and (1) to the outlet. (0.167) and (0.833) at the z*-axis corresponds to the electrode/channel interfaces.

The concentration polarization for the standard case is presented in Fig. 9 for the anode/electrolyte interface and in Fig. 10 for the cathode/electrolyte interface. It is found that the concentration polarization is significant for positions under the interconnect ribs and also that the cathode one is much higher than the anode one. The highest values are found close to the outlet, where the gradients of oxygen and hydrogen in the direction normal to the main flow direction are highest. For the anode also an effect at the inlet due to the anode-supported structure can be seen. It is concluded that at positions under the rib and close to the outlet, the concentration polarization corresponds to around 20% of the total polarizations. At positions under the fuel and air channels the part corresponding to concentration polarization is less than 1 % of the total polarizations. Note that the color scale in Fig. 9 and in Fig. 10 is identical.

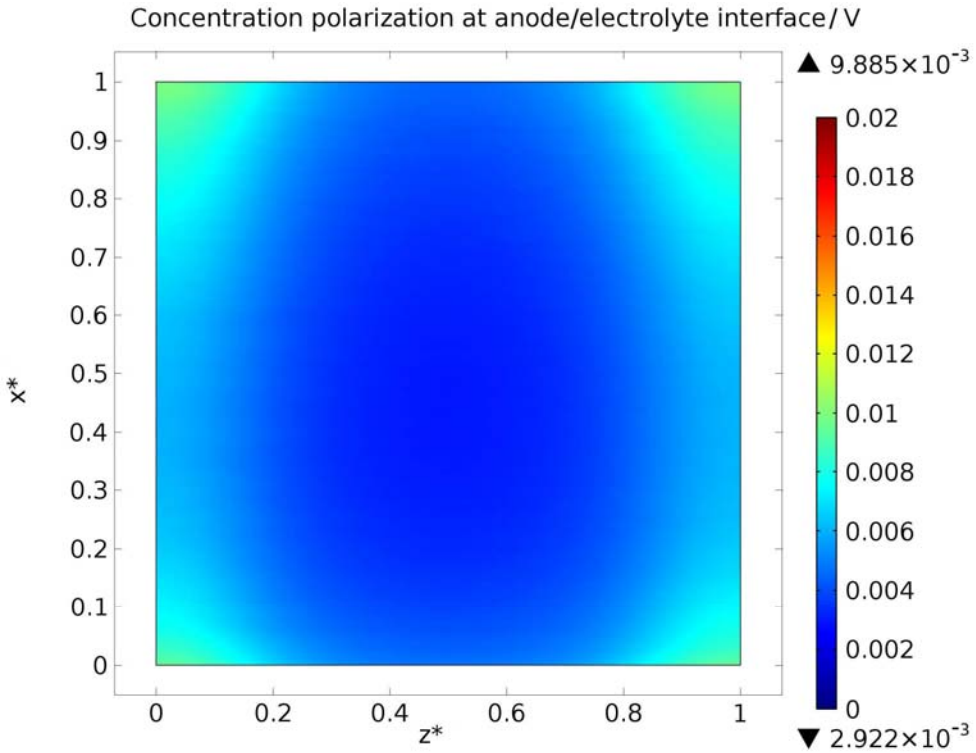

Figure 9. Anode concentration polarization for the standard case. (0) at the x*-axis corresponds to the inlet and (1) to the outlet. (0.167) and (0.833) at the z*-axis corresponds to the electrode/channel interfaces.

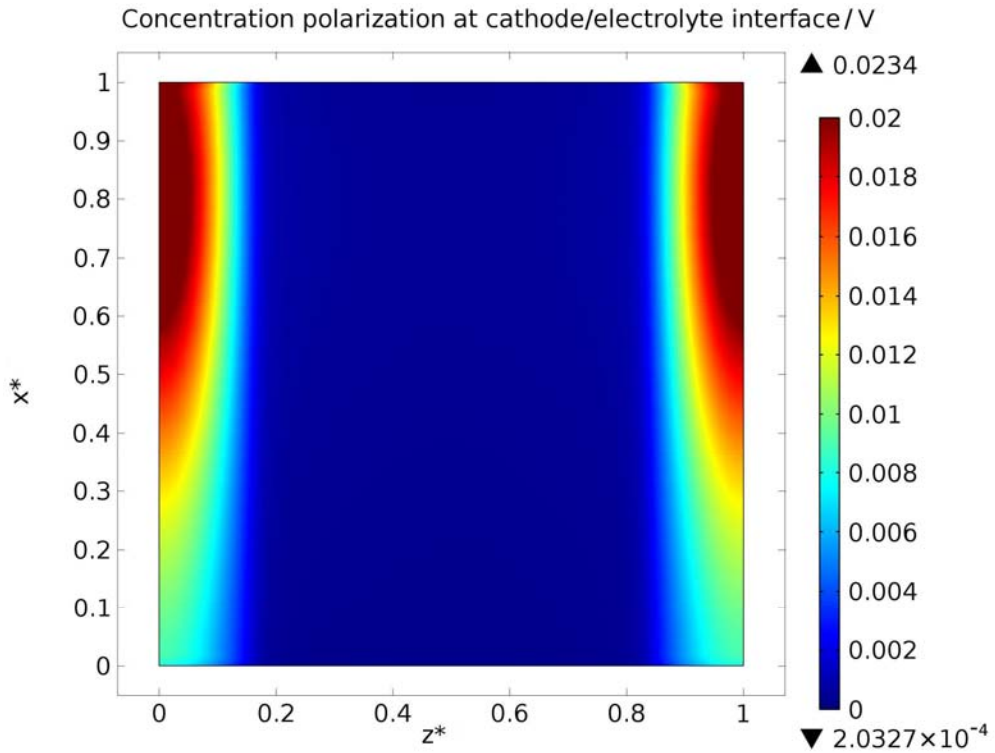

Figure 10. Cathode concentration polarization for the standard case. (0) at the x*-axis corresponds to the inlet and (1) to the outlet. (0.167) and (0.833) at the z*-axis corresponds to the electrode/channel interfaces.

The electric potential at the anode/electrolyte interface and at the cathode/electrolyte is presented in Fig. 11 and Fig. 12, respectively. Note that the color scales differ and 0.70 V in Fig. 12 corresponds to the cell potential. The ohmic polarization due to the electron resistance increases along the main flow direction as the current density increases. It is found that the ohmic polarization due to electron resistance is of the order ten times bigger in the cathode compared to the anode, mainly due to the different thicknesses, which affects the electron transport in the direction normal to the electrode/electrolyte interface (at positions under the channels), i.e., it is clear that the ohmic polarization due to electron transport in the direction through the electrode/electrolyte interfaces is significantly lower compared to in the direction normal to the electrode/electrolyte interface. It is also concluded that for positions in the electrodes under the rib, the electron resistance is almost neglible. The distribution of the

ohmic polarization due to electron transport can be compared to the concentration polarization, which is very low at positions under the air and fuel channels, respectively. Figure 13 presents the electron current density in the z-y plane at the outlet. It is shown that the highest electron current density occurs in the cathode at the air channel/interconnect corners. A similar trend can be seen at the anode/interconnect ribs corner, but the maximum value in the anode is around 40 % of the cathode one. It is clear that the maximum electron current density is more than ten times higher than the maximum ion current density. Note that the electron transport in the direction normal to the cathode/electrolyte interface was not included in our previous 2D models.

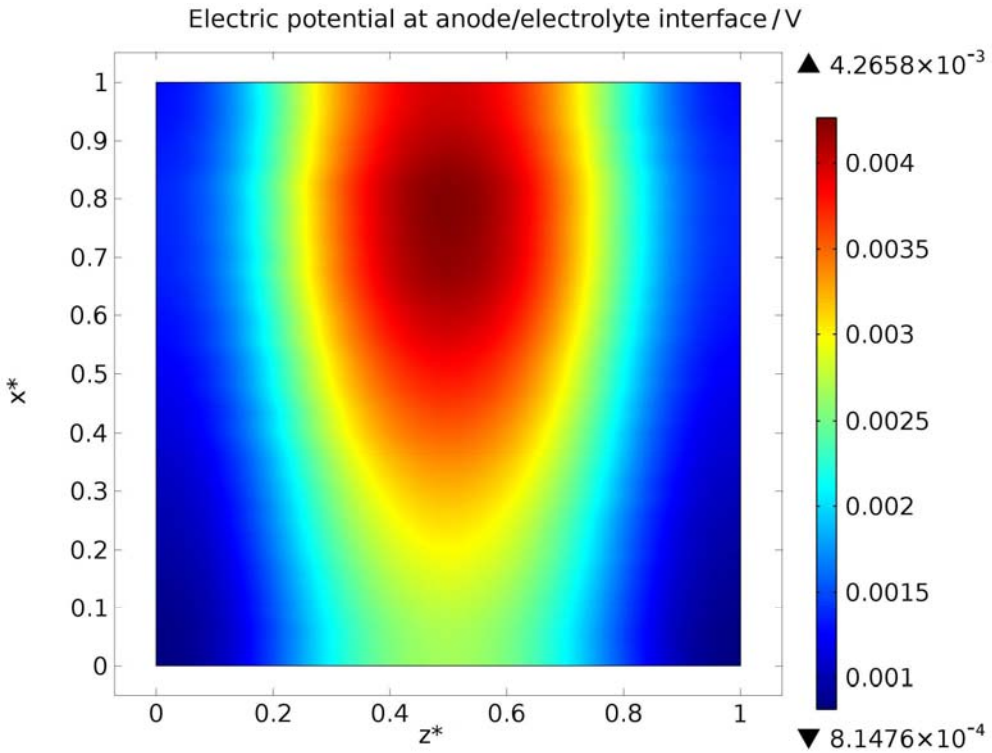

Figure 11. Activation polarization at the anode/electrolyte interface for the standard case. (0) at the x*-axis corresponds to the inlet and (1) to the outlet. (0.167) and (0.833) at the z*-axis corresponds to the electrode/channel interfaces.

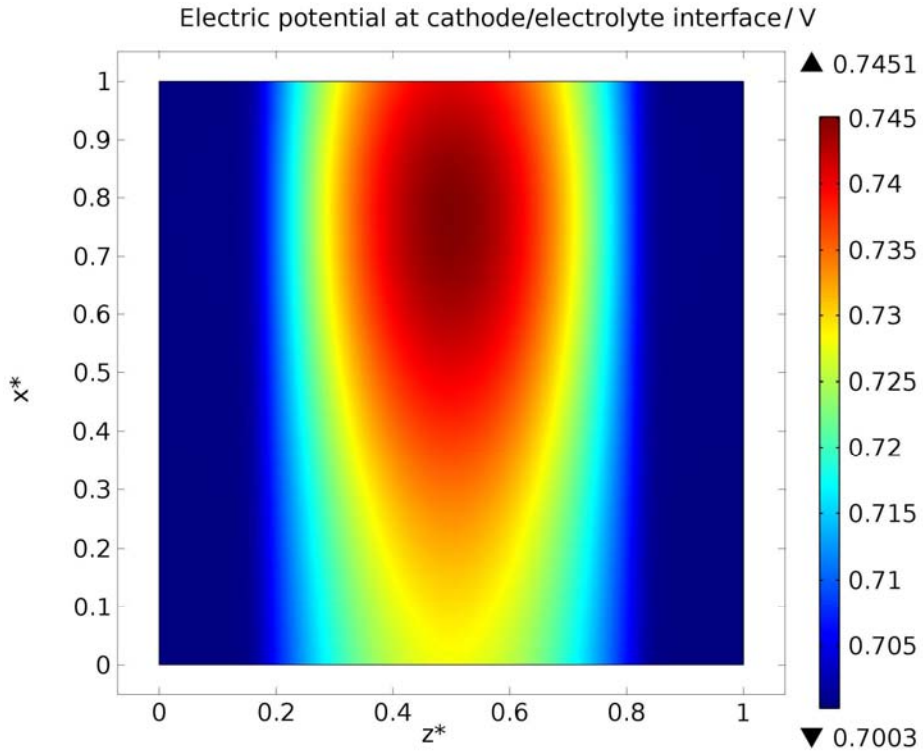

Figure 12. Activation polarization at the cathode/electrolyte interface for the standard case. (0) at the x*-axis corresponds to the inlet and (1) to the outlet. (0.167) and (0.833) at the z*-axis corresponds to the electrode/channel interfaces.

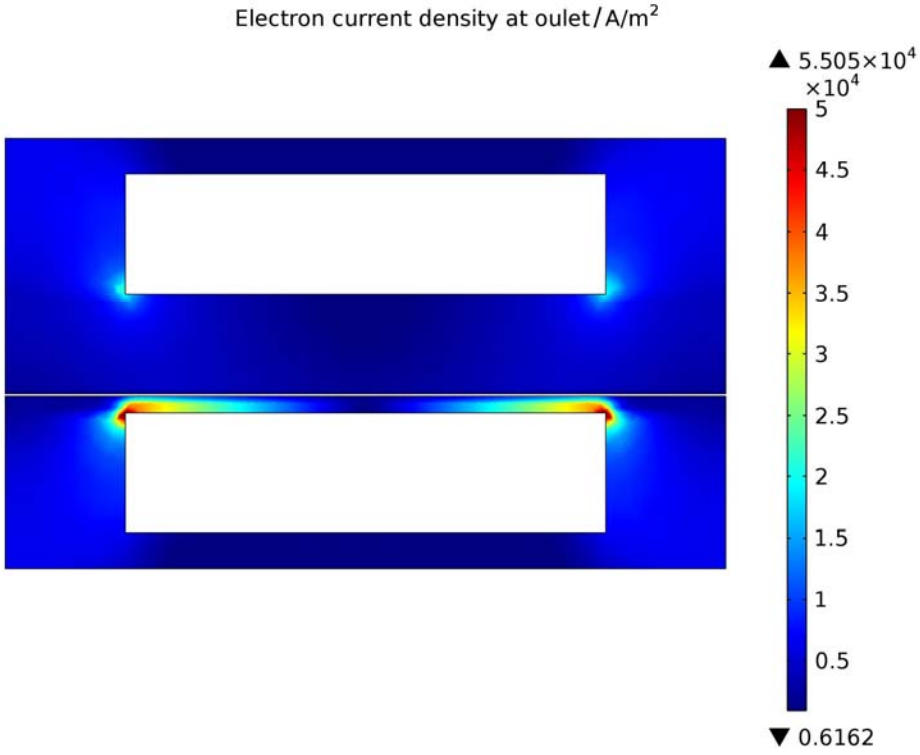

Figure 13. Electron current density in the y-z-plane for the standard case. (0) at the x*-axis corresponds to the inlet and (1) to the outlet. (0.167) and (0.833) at the z*-axis corresponds to the electrode/channel interfaces.

3.2 Decreased cell potential

A decreased operation potential means more "Volt" available for the different polarizations, i.e., the current density increases from an increased activation polarization (within Fig. 14, compared to Fig. 5 for the standard case). The average current density is 2570 A/m^2 (corresponds to a power density of 1800 W/m^2) compared to 2170 A/m^2 for the standard case. The maximum value reaches 4200 A/m^2, compared to 3400 A/m^2. Also the lowest value (close to the inlet) increased off the decreased cell potential (1720 A/m^2 compared to 1560 A/m^2). The increased current density at the inlet results in an increased heat generation along the main flow direction. The higher temperature enables an even higher current density and the increase in current density is accelerated along the main flow direction.

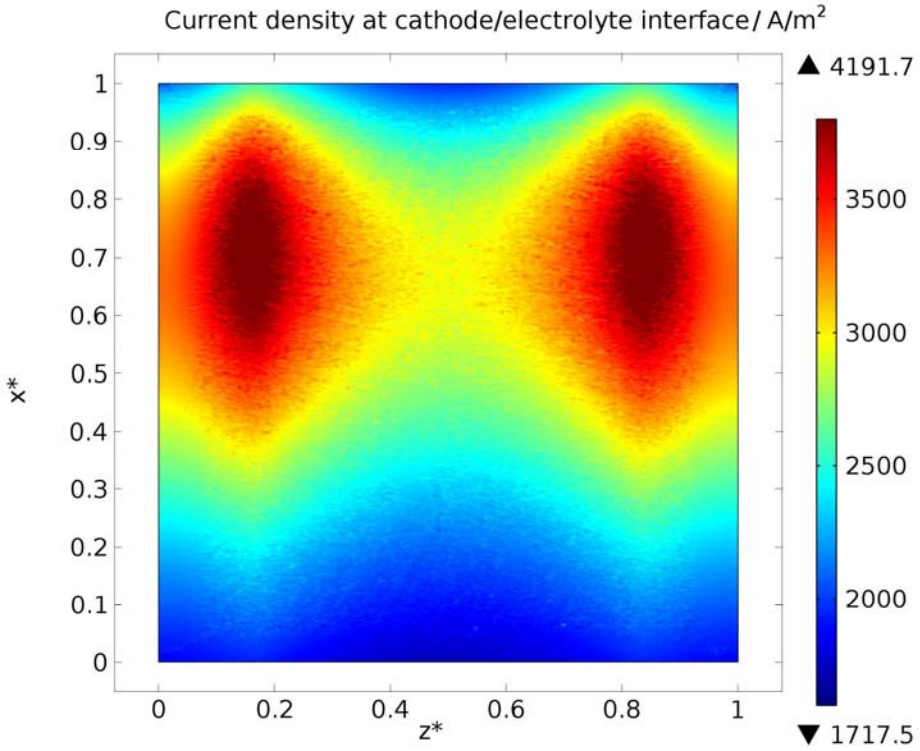

Figure 14. Ion current density for the case with a decreased cell potential. (0) at the x*-axis corresponds to the inlet and (1) to the outlet. (0.167) and (0.833) at the z*-axis corresponds to the electrode/channel interfaces.

The ICV at the inlet is not changed as the cell potential is decreased, as presented in Fig.15. However, the impact on the ICV increases along the main flow direction with a significantly lower ICV at the outlet, compared to the standard case (in Fig. 6). The decreased ICV (along the main flow direction) can be explained by an increased temperature and a decreased concentration of the electrochemical reactants, due to the higher current density predicted from the decreased cell potential.

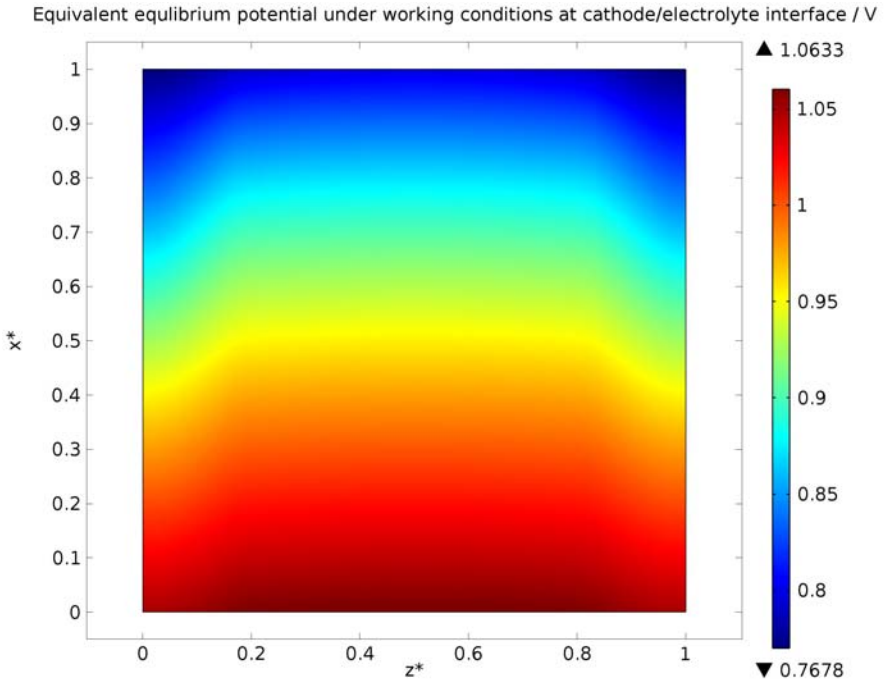

Figure 15. ICV for the case with a decreased cell potential. (0) at the x*-axis corresponds to the inlet and (1) to the outlet. (0.167) and (0.833) at the z*-axis corresponds to the electrode/channel interfaces.

The decreased cell potential enables an increased activation polarization close to the inlet within both the anode (Fig. 16) and cathode (Fig. 17), compared to the standard case (Figs 7-8). On the other hand, at the outlet the activation polarizations are decreased, because the impact from the decreased ICV is bigger than the one from the decreased cell potential. As for the standard case the activation polarization is slightly higher within the anode compared to within the cathode.

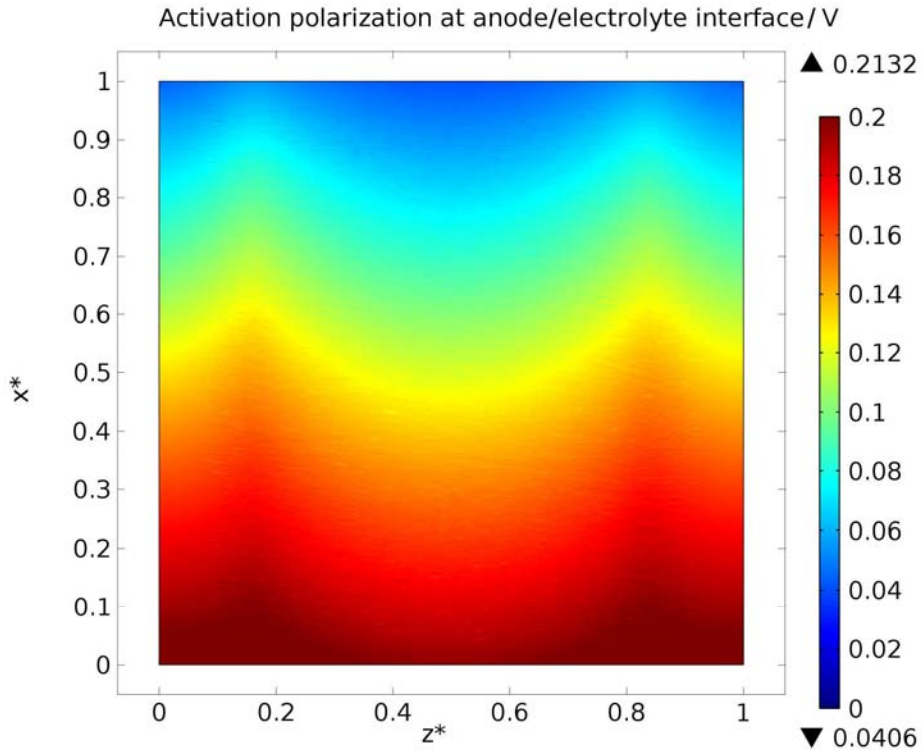

Figure 16. Activation polarization at the anode/electrolyte interface for the case with a decreased cell potential. (0) at the x*-axis corresponds to the inlet and (1) to the outlet. (0.167) and (0.833) at the z*-axis corresponds to the electrode/channel interfaces.

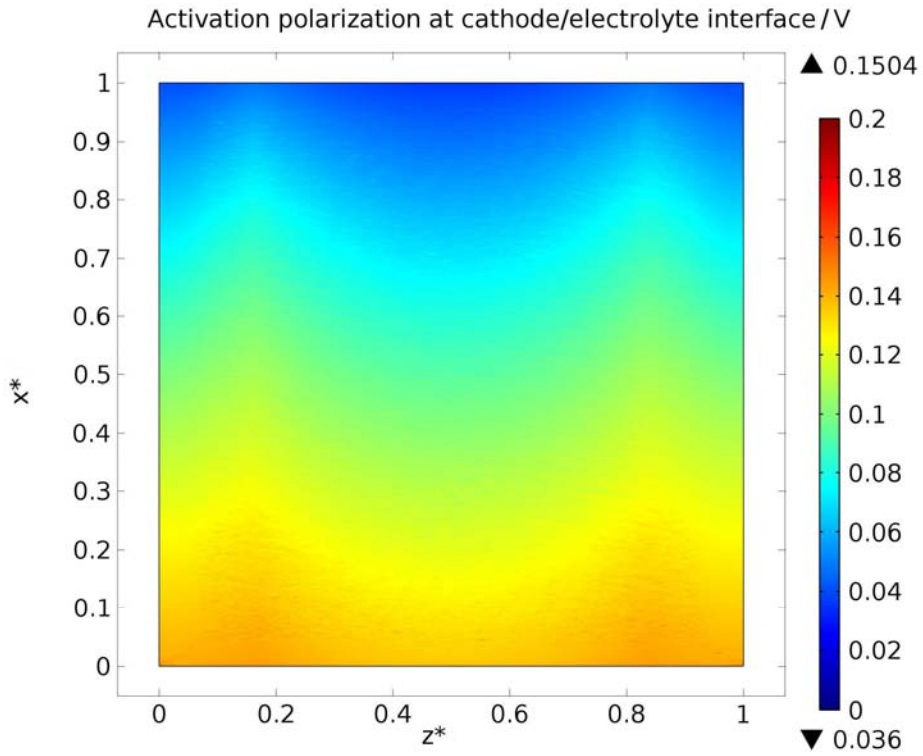

Figure 17. Activation polarization at the cathode/electrolyte interface for the case with a decreased cell potential. (0) at the x*-axis corresponds to the inlet and (1) to the outlet. (0.167) and (0.833) at the z*-axis corresponds to the electrode/channel interfaces.

3.3 Sensitivity on active area-to-volume ratio

The current density (Fig. 18) is significantly increased as the anode AV is increased with a factor of 2 compared to the standard case. Note that for the color scale in Fig. 17, the color between 4000 and 6000 A/m^2 is the same. The difference close to the inlet is relatively small. However, due to the strong coupling between the current density, heat generation and temperature distribution, the current density gradient increases along the main flow direction. The average current density is 2860 A/m^2 (corresponds to a power density of 2000 W/m^2) compared to 2170 A/m^2 for the standard case. The highest current density reaches 6000 A/m^2, compared to 3400 A/m^2. The gradient in the direction normal to the main flow direction (z*-direction) close to the outlet is very steep at positions under the interconnect ribs, due to the gas-phase and electron resistance, mainly within the cathode, because the anode is relatively thick.

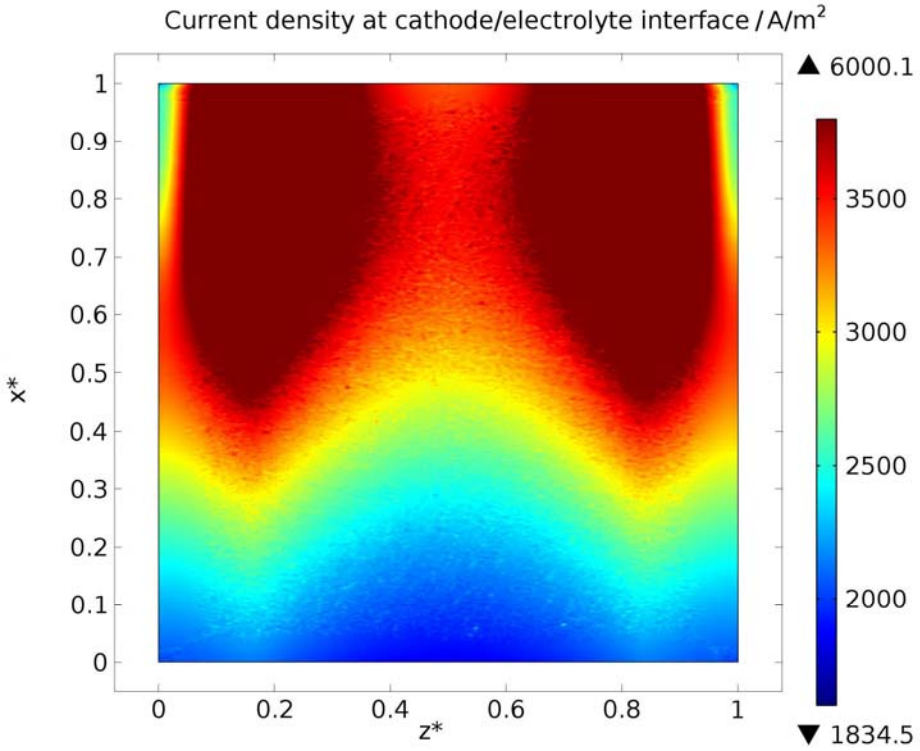

Figure 18. Ion current density for the case with an increased anode AV available for electrochemical reactions. (0) at the x*-axis corresponds to the inlet and (1) to the outlet. (0.167) and (0.833) at the z*-axis corresponds to the electrode/channel interfaces.

The ICV is not changed at the inlet as the anode AV is increased. However, the influence increases strongly along the main flow direction as the temperature increases and the concentration of electrochemical reactants decreases, due to the increased current density. The anode activation polarization (Fig. 19) at the inlet decreased off slightly more than 20 mV (compared to the standard case in Fig. 7), and the cathode activation polarization (Fig. 20) at the inlet increased off slightly less than 20 mV (compared to the standard case in Fig. 8), as the anode AV is increased by a factor of two. The difference between the decrease on the anode side and the increase on the cathode side can be explained from an increased ohmic polarization from the increased current density. Close to the outlet, the gradients in the direction normal to the main flow direction (z*-direction) is significantly increased, compared to the standard case, due to the increased oxygen and hydrogen concentration gradients in the same direction as well as the electron resistance in the interconnect.

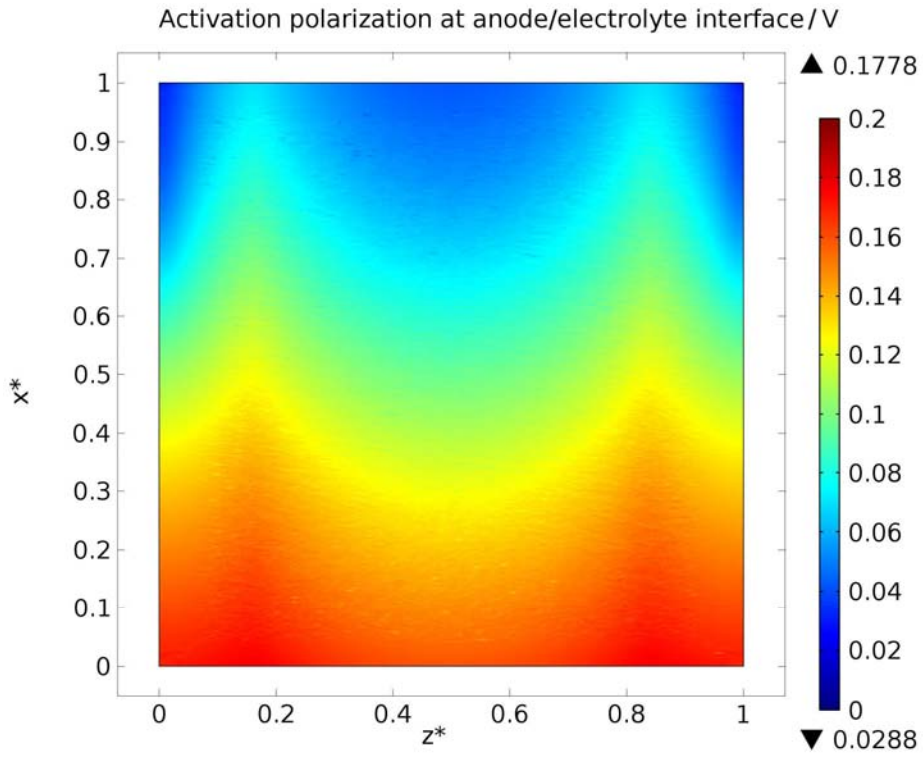

Figure 19. Activation polarization at the anode/electrolyte interface for the case with an increased anode AV available for electrochemical reactions. (0) at the x*-axis corresponds to the inlet and (1) to the outlet. (0.167) and (0.833) at the z*-axis corresponds to the electrode/channel interfaces.

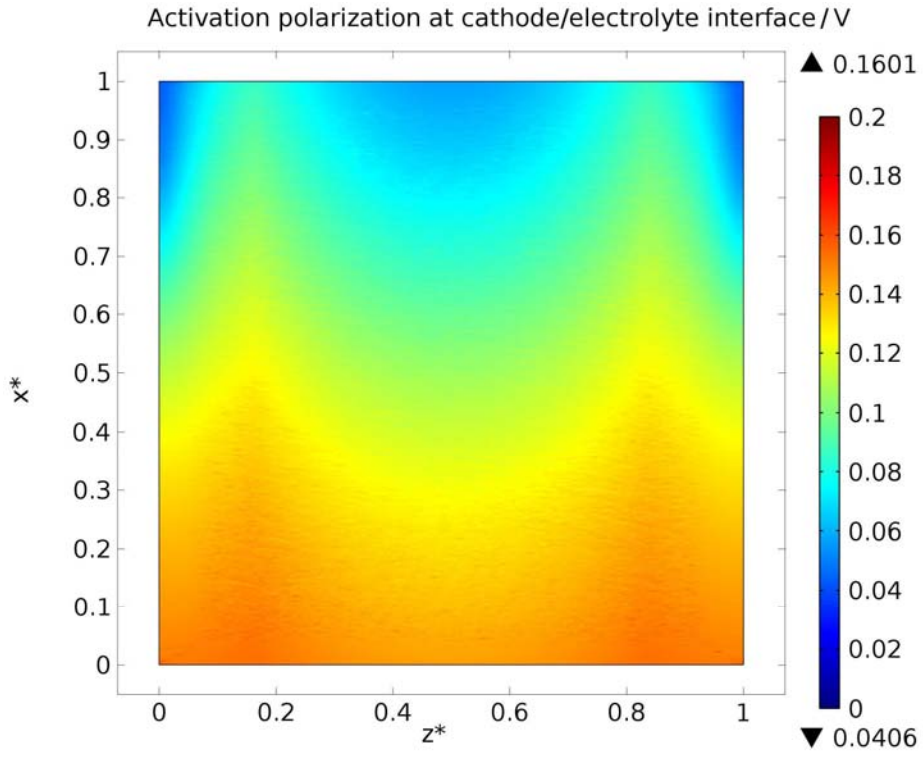

Figure 20. Activation polarization at the cathode/electrolyte interface for the case with an increased anode AV available for electrochemical reactions. (0) at the x*-axis corresponds to the inlet and (1) to the outlet. (0.167) and (0.833) at the z*-axis corresponds to the electrode/channel interfaces.

3.4 Sensitivity on activation energies

In section 2, it is revealed that there exist large discrepancies within the open literature concerning the values for the anode and cathode electrochemical activation energy. The impact from decreased electrochemical activation energies both on the anode side and the cathode side is investigated in Figs. 21-22. The average current density is increased with around 19% as the cathode activation energy is decreased with 7 kJ/mol (or -5%). As the anode activation energy is decreased with 5 % (or 7 kJ/mol) the average current density is increased with 21 %. For our parameter study the inlet temperature, concentration and mass flow rates are kept constant, leading to an increased fuel utilization as the current density increases. For realistic operating the (inlet) fuel mass flow rate would be increased if the fuel utilization becomes too high (i.e., limiting). It is proven that catalytic material optimization reducing the electrochemical activation energies increases the current density strongly. However, the current density gradients along the main flow direction will increase, due to the accelerated coupling with the heat generation from the electrochemical reactions as well as the different polarizations.

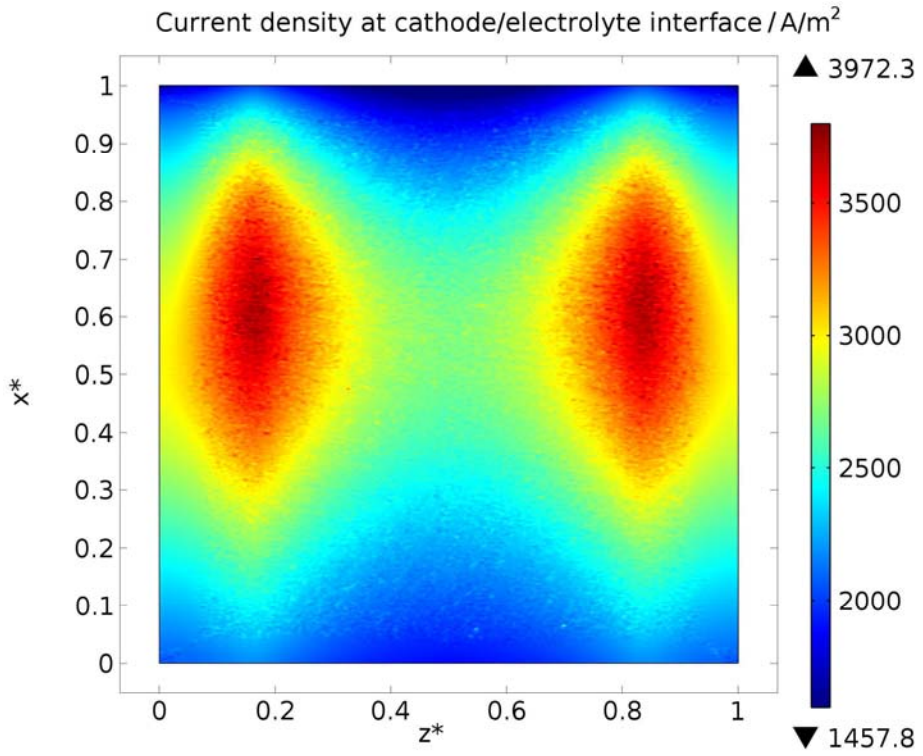

Figure 21. Ion current density for the case with decreased anode electrochemical activation energy. (0) at the x*-axis corresponds to the inlet and (1) to the outlet. (0.167) and (0.833) at the z*-axis corresponds to the electrode/channel interfaces.

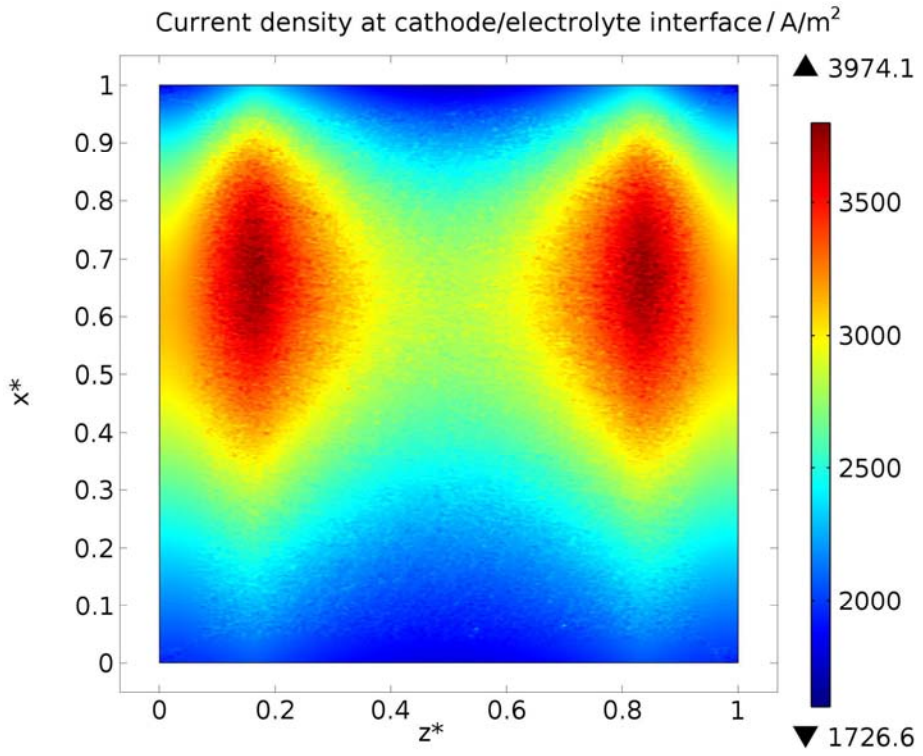

Figure 22. Ion current density for the case with decreased cathode electrochemical activation energy. (0) at the x*-axis corresponds to the inlet and (1) to the outlet. (0.167) and (0.833) at the z*-axis corresponds to the electrode/channel interfaces.

4 Conclusions

A FEM approach is developed to investigate various physical and chemical phenomena, inside a single cell of an anode-supported planar SOFC. Equations for gas-phase species, momentum, heat, electron and ion transport are solved simultaneously, and the couplings with kinetic expressions for electrochemical reactions in the electrodes are included. The electrochemical reactions are implemented as specific source terms in the governing transport equations in the finite region close to the electrode/electrolyte interface.

The current density increases along the main flow direction, due to the temperature rise from the electrochemical reactions. This increase is limited due to the consumption of electrochemical reactants within the cell. It is concluded that a large current density gradient appears in the active electrode regions corresponding to the positions of the ribs between the channels, due to the increased resistance for the oxygen gas-phase and the electron transport. It is clear that the coupling between the local current density and the local temperature is strong, and the increase in current density is accelerated from an increased temperature along the main flow direction. It is noted that at positions under the rib and close to outlet the concentration polarization corresponds to around 20 % of the total polarizations. At positions under the fuel and air channels the part corresponding to concentration polarization is less than 1 % of the total polarization. It is concluded that for positions (in the electrodes) close to the rib, the electron resistance is almost neglible.

The connection between the electrode active area-to-volume ratios and the corresponding activation polarization is shown. An increase of the anode active area-to-volume ratio with a factor of two transfers around 20 mV of polarization from the anode to the cathode side,

under the circumstances investigated in this study. The coupling between the electrochemical activation energies and the current density distribution is shown in this paper. A decrease of the cathode activation energy with 5 % increases the average current density with 19 % and a decrease of the anode activation energy with 5 % increases the average current density with 21 % (keeping the inlet temperature, concentrations and flow rates constant).

Modeling is key component in the SOFC development beyond the current state-of-the-art, because it is beneficial to understand the mechanisms of various inter-played phenomena and effects on the cell performance. It is also hard to measure the local parameters inside an SOFC, particularly inside the small scale functional materials. due to the high operating temperature as well as the fact that SOFC are contained in a sealed box. Modeling and simulation of SOFC charge transfer and electrochemical performance are critical to enable optimization of the geometry and performance. For macroscale modeling the micro structure related properties defining the porous media, for example, the porosity, tortuosity factor and specific area available for surface reactions, are required, The coupling to models in the smaller scales will increase the scientific value of the macroscale CFD models. Future challenges include:

- Improved scientific understanding of the hydrogen electrochemical detailedkinetics for SOFC anodes and cathodes, i.e., to present more accurate activation energies and active area-to-volume ratios.
- To develop a graded electrode structure in several direction for superior (electrochemical) performance.
- Enhanced scientific knowledge concerning the importance of carbon monoxide as an electrochemical active species (when a fuel containing carbon monoxide is supplied).

- Determining the detailed methane steam reforming kinetics for SOFC anodes (when a fuel containing methane is supplied).

5 Nomenclature

AV	active surface area-to-volume ratio [$m^2\ m^{-3}$]
c_p	specific heat at constant pressure [$J\ kg^{-1}\ K^{-1}$]
D_{ij}	effective (ordinary) diffusivity [$m^2\ s^{-1}$]
$D_{ij,eff}$	average effective diffusivity [$m^2\ s^{-1}$]
$D_{k,ij}$	effective Knudsen diffusivity [$m^2\ s^{-1}$]
D_i^T	thermal diffusion coefficient [$kg\ m^{-1}\ s^{-1}$]
E	activation energy [$kJ\ mol^{-1}$], (actual) operating potential [V]
E^0	open-circuit potential at standard pressure [V]
F	Faradays constant [96 485 $A\ s\ mol^{-1}$]
F	volume force vector [$N\ m^{-3}$]
I	current density [$A\ m^{-2}$]
i_0	exchange current density [$A\ m^{-2}$]
k	thermal conductivity [$W\ m^{-1}\ K^{-1}$]
k_e''	pre-exponential factor [$\Omega^{-1}m^{-2}$]
L	cell length (along the main flow direction) [m]
n_e	number of electrons transferred per reaction [-]
p	pressure [atm or Pa]
Q_h	*s*ource term (heat) [$W\ m^{-3}$]
R	gas constant [$8.3145\ J\ mol^{-1}\ K^{-1}$]
S	entropy change due to chemical reaction [$J\ mol^{-1}\ K^{-1}$]
S_i	source term, [$kg\ m^{-3}\ s^{-1}$)]
T	temperature [K]
$\vec{u}$	velocity vector [$m\ s^{-1}$]
x	mole fraction [-]
V	volume fraction for the specific materials [-]
w	mass fraction [-]
W	width of one fuel/air channel and the corresponding ribs [m]

5.1 Greek symbols

ε	porosity [-]
η	polarization [V]
κ	permeability [m^2]
μ	dynamic viscosity [Pa s]
ρ	density [kg/m^3]
σ	ion/electron conductivity [$\Omega^{-1}\ m^{-1}$]
τ	tortuosity factor [-]
ϕ	electric potential [V]
Ψ	viscous stress tensor, [$N\ m^{-2}$]

5.2 Abbreviations, Subscripts and Superscripts

a	anode
act	activation (polarization)
b	electrode/gas channel interface
c	cathode
CFD	computational fluid dynamics
conc	concentration (polarization)
FEM	finite element method
i,j	species index
ICV	ideal condition potential
l	ion transfer material
NIMTE	Ningbo Institute of Material Technology and Engineering, China
ohm	ohmic (polarization)
s	electron transfer material
SOFC	solid oxide fuel cell
TPB	three-phase boundary

5.3 Chemical

e^-	electron
H_2	hydrogen (gas phase molecule)
H_2O	water (gas phase molecule)
Ni	nickel

O_2 oxygen (gas phase molecule)

O^{2-} oxygen ion

YSZ yttria-stabilized zirconia

6 Acknowledgments

The financial support from the Swedish Research Council (VR-621-2010-4581) and the European Research Council (ERC-226238-MMFCs) is gratefully acknowledged.

References

[1] Y.-L. He, W.-Q. Tao, Multiscale Simulations of Heat Transfer and Fluid Flow Problems, ASME J. Heat Transfer 134 (2012) 031018.

[2] M. Andersson, Solid Oxide Fuel Cell Modeling at the Cell Scale - Focusing on Species, Heat, Charge and Momentum Transport as well as the Reaction Kinetics and Effects, Doctoral dissertation, ISBN 9789174731804, Lund University, 2011.

[3] M. Peksen, R. Peters, L. Blum, D. Stolten, Numerical Modelling and Experimental Validation of a Planar Type Pre-Reformer in SOFC Technology, Int. J. Hydrogen Energy 34 (2009) 6425-6436.

[4] K.N. Grew, W.K.S. Chiu, A Review of Modeling and Simulation Techniques across the Length Scales for the Solid Oxide Fuel Cell, J. Power Sources 199 (2012) 1-13.

[5] M. Andersson, J. Yuan, B. Sundén, Review on Modeling Development for Multi-scale Chemical-Reactions-Coupled Transport Phenomena in SOFCs, J. Applied Energy 87 (2010) 1461-1476.

[6] J. Park, P. Li, J. Bae, Int. J., Analysis of Chemical, Electrochemical Reactions and Thermo-Fluid Flow in Methane-Feed Internal Reforming SOFCs: Part II-Temperature Effect, Hydrogen Energy 37 (2012) 8532-8555.

[7] M. Andersson, J. Yuan, B. Sundén, SOFC Modeling Considering Electrochemical Reactions at the Three Phase Boundaries, Int. J. Heat Mass Transfer 55 (2012) 773-788.

[8] W.G. Bessler, M. Vogler, H. Störmer, D. Gerthsen, A. Utz, A. Weber, E. Ivers-Tiffée, Model Anodes and Anode Models for Understanding the Mechanism of Hydrogen Oxidation in Solid Oxide Fuel Cells, Phys. Chem. Chem. Phys. 12 (2010) 13888-13903.

[9] M. Liu, M. Lynch, K. Blinn, F. Alamgir, Y. Choi, Rational SOFC Material Design: New Advances and Tool, Materials Today 14 (2011) 534-546.

[10] M. Andersson, J. Yuan, B. Sundén, Grading the Amount of Electrochemical Active Sites along the Main Flow Direction of an SOFC, J. Electrochemical Soc. 160 (2013) F1-F12.

[11] L. Liu, R. Flesner, G.-Y. Kim, A. Chandra, Modeling of Solid Oxide Fuel Cells with Particle Size and Porosity Grading in Anode Electrode, Fuel Cells 12 (2012) 97-108.

[12] Z. Cheng, J.-H. Wang, Y.M. Choi, L. Yang, M.C. Lin, M. Liu, From Ni-YSZ to Sulfur-Tolerant Anodes: Electrochemical Behavior, Modeling, In Situ Characterization, and Perspectives, Energy Environ. Sci. 4 (2011) 4380-4409.

[13] H. Miao, W.G. Wang, T.S. Li, T. Chen, S.S. Sun, C. Xu, Effects of Coal Syngas Major Compositions on Ni/YSZ Anode-Supported Solid Oxide Fuel Cells, J. Power Sources 195 (2010) 2230-2235.

[14] T.S Li, C. Xu, T. Chen, H. Miao, W.G. Wang, Chlorine Contaminants Poisoning of Solid Oxide Fuel Cells, J. Solid State Electrochem. 15 (2011) 1077-1085.

[15] S. Kakaç, A. Pramuanjaroenkij, X.Y. Zhou., A Review of Numerical Modeling of Solid Oxide Fuel Cells, J. Hydrogen Energy 32 (2007) 761-786.

[16] K.N. Grew, A.S. Joshi, A.A. Peracchio, W.K.S. Chiu, Pore-Scale Investigation of Mass Transport and Electrochemistry in a Solid Oxide Fuel Cell Anode, J. Power Sources 195 (2010) 2331-2345.

[17] W.Y. Lee, D. Wee, A.F. Ghoniem, An Improved One-Dimensional Membrane-Electrode Assembly Model to Predict the Performance of Solid Oxide Fuel Cell including the Limiting Current Density, J. Power Sources 186 (2009) 417-427.

[18] A. Bertei, A. Barbucci, M.P. Carpanese, M. Viviani, C. Nicolella, Morphological and Electrochemical Modeling of SOFC Composite Cathodes with Distributed Porosity, Chem. Engineering 207-208 (2012) 167-174.

[19] J. Shi, X. Xue, Inverse Approach to Quantify Multi-Physicochemical Properties of Porous Electrodes for Solid Oxide Fuel Cells, Electrochim. Acta 56 (2011), 8718-8726.

[20] Y. Patcharavorachot, A. Arpornwichanop, A. Chuachuebsuk, Electrochemical Study of a Planar Solid Oxide Fuel Cell: Role of Support Structures, J. Power Sources 177 (2008) 254-261.

[21] S. Sohn, J.H. Nam, D.H. Jeon, C.J. Kim, A Micro/Macroscale Model for Intermediate Temperature Solid Oxide Fuel Cells with Prescribed Fully-Developed Axial Velocity Profile in Gas Channels, Int. J. Hydrogen Energy 35 (2010) 11890-11907.

[22] P. Aguiar, C.S. Adjiman, N.P. Brandon, Anode-Supported Intermediate Temperature Direct Internal Reforming Solid Oxide Fuel Cell. I: Model-Based Steady-State Performance, J. Power Sources 138 (2004) 120-136.

[23] W.G. Bessler, S. Gewies, M. Vogler, A New Framework for Detailed Electro-Chemical Modeling of Solid Oxide Fuel Cells, Electrochim. Acta 53 (2007) 1782-1800.

[24] H. Xiao, T.L. Reitz, M.A. Rottmayer, Polarization Measurements of Anode-Supported Solid Oxide Fuel Cells Studied by Incorporation of a Reference Electrode, J. Power Sources 183 (2008) 46-54.

[25] M. Andersson, H. Paradis, J. Yuan, B. Sundén, Modeling Analysis of Different Renewable Fuels in an Anode Supported SOFC, J. Fuel Cell Science and Technology 8 (2011) 031013.

[26] Fuel Cell Handbook (7th edition), U.S. DoE, Morgantown, West Virginia, 2004.

[27] W. Winkler, P. Nehter, Thermodynamics of Fuel Cells, Fuel Cells and Hydrogen Energy 1 (2008) 15-50.

[28] A.S. Joshi, A.A. Peracchio, K.N. Grew, W.K.S. Chiu, Lattice Boltzmann Method for Multi-Component, Non-Continuum Mass Diffusion, J. Phys. D: Appl. Phys. 40 (2007) 7593-7600.

[29] H. Paradis, M. Andersson, J. Yuan, B. Sundén, CFD Modeling considering Different Kinetic Models for Internal Reforming Reactions in an Anode-Supported SOFC, J. Fuel Cell Science and Technology 8 (2011) 031014.

[30] S.B. Beale, Numerical Models for Planar Solid Oxide Fuel Cells, Transport Phenomena in Fuel Cells, B. Sundén and M. Faghri (eds.), WIT Press (2005) 42-82.

[31] J. Newman, K.E. Thomas-Alyea, Electrochemical Systems, Third Edition, Hoboken, N.J., Wiley-Interscience, 2004.

[32] P. Hofmann, K.D. Panopoulos, L.E. Fryda, E. Kakaras, Comparison between Two Methane Reforming Models Applied to a Quasi-Two-Dimensional Planar Solid Oxide Fuel Cell Model, Energy 34 (2008) 2151-2157.

[33] N. Akhtar, S.P. Decent, K. Kendall, Numerical Modelling of Methane-Powered Micro-Tubular, Single-Chamber Solid Oxide Fuel Cell, J. Power Sources 195 (2010) 7796-7807.

[34] Y. Shi, N. Cai, C. Li, C. Bao, E. Croiset, J. Qian, Q. Hu, S. Wang, Modeling of an Anode-Supported Ni-YSZ|Ni-ScSZ|ScSZ|LSM-ScSZ Multiple Layers SOFC Cell Part I. Experiments, Model Development and Validation, J. Power Sources 172 (2007) 235-245.

[35] A.V. Akkaya, Electrochemical Model for Performance Analysis of a Tubular SOFC, Int. J. Energy Research 31 (2007) 79-98.

[36] A. Konno, H. Iwai, K. Inuyama, A. Kuroyanagi, M. Saito, H. Yoshida, K. Kodani, K. Yoshikata, Mesoscale-Structure Control at Anode/Electrolyte Interface in Solid Oxide Fuel Cell, J. Power Sources 196 (2011) 98-109.

[37] W.G. Bessler, J. Warnatz, D.G. Goodwin, The Influence of Equilibrium Potential on the Hydrogen Oxidation Kinetics of SOFC Anodes, Solid State Ionics 177 (2007) 3371-3383.

[38] J.R. Ferguson, J.M. Fiard, R. Herbin, Three Dimensional Numerical Simulation for Various Geometries of Solid Oxide Fuel Cells, J. Power Sources 58 (1996) 109-122.

[39] S.A. Hajimolana, M.A. Hussain, W.M.A.W. Daud, M. Soroush, A. Shamiri, Mathematical Modeling of Solid Oxide Fuel Cells: A Review, Renewable and Sustainable Energy Reviews 15 (2011) 1893-1917.

[40] D. Kanno, N. Shikazono, N. Takagi, K. Matsuzaki, N. Kasagi, Evaluation of SOFC Anode Polarization Simulation Using Three-Dimensional Microstructures Reconstructed by FIB Tomography, Electrochim. Acta 56 (2011) 4015-4021.

[41] J. Yuan , B. Sundén, Analysis of Chemically Reacting Transport Phenomena in an Anode Duct of Intermediate Temperature SOFCs, ASME J. Fuel Cell Sci. Technol. 3 (2006) 687-701.

[42] J. Yuan, Y. Huang, B. Sundén, W.G. Wang, Analysis of Parameter Effects on Chemical Reaction Coupled Transport Phenomena in SOFC Anodes, Heat Mass Transfer 45 (2009) 471-484.

[43] R. Bove, S. Ubertini, Modeling Solid Oxide Fuel Cell Operation: Approaches, Techniques and Results, J. Power Sources 159 (2006) 543-559.

[44] M. le Bars, M.G. Worster, Interfacial Conditions Between a Pure Fluid and a Porous Medium, Implications for Binary Alloy Solidification, J. Fluid Mech. 550 (2006) 149-173.

[45] COMSOL Multiphysics version 4.3 user guide, Stockholm, Sweden, 2012.

[46] R.C. Reid, J.M. Prausnitz, B.E. Poling, The Properties of Gases & Liquids (fourth edition), McGraw-Hill Book Company, New York, USA, 1987.

[47] D.Y. Murzin, T. Salmi, Catalytic Kinetics, Elsevier Science, 2005.

[48] Kanno D., Shikazono N., Takagi N., Matsuzaki K., Kasagi N., Evaluation of SOFC Anode Polarization Simulation using Three-Dimensional Microstructures Reconstructed by FIB Tomography, Electochim. Acta 56 (2011) 4015-4021.

[49] H. Iwai, N. Shikazono, T. Matsui, H. Teshima, M. Kishimoto, R. Kishida, D. Hayashi, K. Matsuzaki, D. Kanno, M. Saito, H. Muroyama, K. Eguchi, N. Kasagi, H. Yoshida, Quantification of SOFC Anode Microstructure based on Dual Beam FIB-SEM Technique, J. Power Sources 195 (2010) 955-961.

[50] N. Vivet, S. Chupin, E. Estrade, T. Piquero, P.L. Pommier, D. Rochais, E. Bruneton, 3D Microstructural Characterization of a Solid Oxide Fuel Cell Anode Reconstructed by Focused Ion Beam Tomography, J. Power Sources 196 (2011) 7541-7549.

[51] B. Todd, J.B. Young, Thermodynamic and Transport Properties of Gases for use in Solid Oxide Fuel Cell Modeling, J. Power Sources 110 (2002)186-200.

[52] B. Kenny, K. Karan, Engineering of Microstructure and Design of a Planar Porous Composite SOFC Cathode: A Numerical Analyses, Solid State Ionics 178 (2007) 297-306.